Joshua S. Shimony, MD, PhD
Robert C. McKinstry, MD, PhD
Erbil Akbudak, PhD
Joseph A. Aronovitz, MD, PhD
Abraham Z. Snyder, PhD, MD
Nicolas F. Lori, BS
Thomas S. Cull, PhD
Thomas E. Conturo, MD, PhD

Index terms:
Brain, diffusion, 10.99
Brain, gray matter, 10.92
Brain, MR, 10.121411, 10.121416, 10.12144
Brain, white matter, 10.92
Magnetic resonance (MR), diffusion study, 10.12144

Radiology 1999; 212:770–784

Abbreviations:
A_{major} = anisotropy variation in ellipsoid shape along major axis
A_{minor} = anisotropy variation in ellipsoid shape along minor axis
A_σ = total anisotropy
AW_{ortho} = orthogonal anisotropy-weighted index
AW_{tet} = tetrahedral anisotropy-weighted index
f_{ortho} = fraction of anisotropy in AW_{ortho}
f_{tet} = fraction of anisotropy in AW_{tet}
GM = gray matter
ROI = region of interest
SNR = signal-to-noise ratio
WM = white matter

[1] From the Mallinckrodt Institute of Radiology (J.S.S., R.C.M., E.A., J.A.A., A.Z.S., T.S.C.) and Dept of Physics (N.F.L., T.E.C.), Washington University Medical Center, 510 S Kingshighway Blvd, St Louis, MO 63110. Received Jul 20, 1998; revision requested Aug 19; revision received Nov 10; accepted Jan 15, 1999. Supported in part by grants from Major Grants Program of McDonnell Center for Higher Brain Function, National Multiple Sclerosis Society Pilot Research Award, Charles A. Dana Foundation Consortium on Neuroimaging Leadership Training, and PRAXIS III Fellowship from the Portuguese government. J.S.S. supported by RSNA Research and Education Foundation Research Resident Grant. **Address reprint requests to** J.S.S. (e-mail: *shimonyj@npg.wustl.edu*).

© RSNA, 1999

Author contributions:
Guarantors of integrity of entire study, J.S.S., T.E.C.; study concepts, T.E.C., R.C.M.; study design, T.E.C., R.C.M., J.S.S.; definition of intellectual content, all authors; literature research, J.S.S., T.E.C.; experimental studies, R.C.M., T.E.C., J.S.S.; data acquisition, R.C.M., E.A., J.S.S., T.E.C.; data analysis, J.S.S., A.Z.S., J.A.A., T.S.C., N.F.L., R.C.M., T.E.C.; statistical analysis, J.S.S., T.E.C.; manuscript preparation and review, J.S.S., T.E.C.; manuscript editing, T.E.C., J.S.S., R.C.M.

Quantitative Diffusion-Tensor Anisotropy Brain MR Imaging: Normative Human Data and Anatomic Analysis[1]

PURPOSE: To obtain normative human cerebral data and evaluate the anatomtomic information in quantitative diffusion anisotropy magnetic resonance (MR) imaging.

MATERIALS AND METHODS: Quantitative diffusion anisotropy MR images were obtained in 13 healthy adults by using single-shot echo-planar MR imaging and a combination of tetrahedral and orthogonal gradient encoding (whole-brain coverage in about 1 minute). White matter (WM) anatomy was assessed at visual inspection, and values were measured in various brain regions. Different anisotropy measures, including total anisotropy (A_σ), were compared on the basis of information content, rotational invariance, and susceptibility to noise. Partial volume and noise effects were simulated.

RESULTS: Anisotropy MR images depicted WM features not typically seen on conventional MR images (eg, external capsule, thalamic substructures, basal ganglia, occipital WM, thickness of the internal capsule). Statistically significant anisotropy differences occurred across brain regions, which were reproducible within and across subjects. A_σ was highest in commissural WM and progressively lower in projection and association WM. This order paralleled that of known resistance to spread of vasogenic edema, which suggested that anisotropy may be sensitive to WM histologic structure. Gray matter (GM) A_σ data were consistent with zero anisotropy, and partial volume WM-GM effects were approximately linear. A_σ image quality could be effectively improved by means of averaging.

CONCLUSION: Quantitative diffusion anisotropy images can be obtained rapidly and demonstrate subtle WM anatomy. Different histologic types of WM have significant and reproducible anisotropy differences.

Random diffusive motion of water along the direction of a strong field gradient will cause spin dephasing in magnetic resonance (MR). As shown by Stejskal and Tanner (1), quantitative diffusion coefficients can be measured with MR by encoding diffusion with balanced gradients applied before and after a spin-echo refocusing pulse and comparing this signal loss to a reference signal acquired with no diffusion encoding. The amount of diffusion sensitivity is indicated by the *b* factor, which is dependent on the timing and strength of the diffusion-encoding gradients.

MR imaging of diffusion effects with a combination of spin-echo imaging and Stejskal-Tanner gradients was used by Le Bihan and colleagues (2,3) and by Taylor and Bushell (4). The technique of echo-planar MR imaging (5) has been particularly useful for acquisition of diffusion information, as demonstrated by Avram and Crooks (6), Turner and colleagues (7,8), and McKinstry et al (9).

In early human diffusion MR imaging studies (10,11), it was realized that water diffusion is anisotropic in many biologic media such as white matter (WM) and muscle (ie, the rate of water diffusion varies with direction). Anisotropic diffusion can, in general, be represented by a symmetric 3 × 3 diffusion tensor D at each position in space (12,13) and can be modeled as ellipsoidal water displacements (12), as was suggested by Basser et al (14) for

modeling of MR image data. Anisotropy is a quantitative parameter that represents the degree to which diffusion varies in different directions. The authors of more recent studies (15,16) have demonstrated the benefit of removal of anisotropic diffusion effects by creating a directionally averaged diffusivity. However, anisotropic diffusion effects provide anatomic information in regions of WM (11,17–19) and may provide diagnostic information for certain WM diseases (20), including multiple sclerosis (21–23). Unlike averaged diffusivity, measures of anisotropy in humans have been shown to be different in various regions of the normal adult brain (17,19) and to vary with gestational age in neonates (24) and with postnatal age in the first several months of life (25).

A number of anisotropy measures have been proposed in the literature (16,26–29). The theoretic basis and advantages of several of these will be discussed. In our study, quantitative anisotropy images were computed from echo-planar MR imaging data (30) that sampled the diffusion tensor along four tetrahedral directions (26) and three coordinate axes. Anatomic findings and anisotropy values are presented from different regions of interest (ROIs) in the normal human brain. The purpose of our study was to obtain normative human cerebral data and evaluate the anatomic information in quantitative diffusion anisotropy MR imaging.

MATERIALS AND METHODS

Theory

In the general case of homogeneous anisotropic media, the diffusion tensor can be represented by a 3×3 matrix. For Gaussian diffusion, the matrix is symmetric (12) and is completely characterized by six scalars: three diagonal elements, D_{xx}, D_{yy}, D_{zz}, and three off-diagonal elements, D_{xy}, D_{xz}, D_{yz}. An ellipsoid, whose surface represents the root mean square diffusive displacement, provides a convenient pictorial representation of anisotropic diffusion in a voxel (14,26,27). Measurement of the diffusion tensor is then equivalent to sampling of enough discrete points on the ellipsoid surface so that the ellipsoid can be uniquely defined (31). Individual elements of the diffusion tensor are not rotationally invariant and, as markers of brain pathologic conditions, have been shown to be misleading in comparison with invariant measures (15,29). In contrast, the trace of the diffusion tensor is invariant under rotations of the coordinate system and is the basis for the directionally averaged diffusivity $\overline{D} = (D_{xx} + D_{yy} + D_{zz})/3$.

Each voxel has a unique principal ellipsoid coordinate system (x', y', z') that, in general, is rotated with respect to the laboratory coordinate system (27). This principal coordinate system lies along the major and minor axes of the diffusion ellipsoid, and, in this rotated system, the diffusion tensor is diagonal. The diagonal matrix elements are the principal diffusivities of the rotated coordinate system $\lambda_{x'}$, $\lambda_{y'}$, and $\lambda_{z'}$ and are the eigenvalues of the diffusion tensor. In the laboratory, the six scalars that represent the diffusion tensor can be expressed in terms of the three eigenvalues ($\lambda_{x'}$, $\lambda_{y'}$, and $\lambda_{z'}$) that are rotationally invariant and the three Euler angles (ϕ, θ, ψ) that describe the relative rotation between the principal and laboratory coordinates (26).

Multiple measures of tissue anisotropy have been proposed (16,26–29). An ideal measure of anisotropy should be quantitative and rotationally invariant. It is desirable that it be a function of the directly measured diffusion coefficients, because any diagonalization of the diffusion tensor and evaluation of its eigenvalues may introduce additional noise. Furthermore, it is advantageous to use anisotropy calculations that are not dependent on sorting of the eigenvalues according to size, because this can introduce additional uncertainty (29), especially in regions with low anisotropy or a low signal-to-noise ratio (SNR). Finally, to facilitate comparison across sequences, institutions, and clinical and basic science disciplines, it would be preferable if anisotropy measures were on an absolute anisotropy scale.

The natural choices for anisotropy measures are A_{major} and A_{minor} (26), which describe the variation in ellipsoid shape along the major and minor axes, respectively. These are obtained by decomposing the diffusion tensor into isotropic and anisotropic components in the x', y', z' ellipsoid coordinate system (26):

$$A_{major} = \frac{1}{3\bar{\lambda}}\left[\lambda_{z'} - \frac{\lambda_{x'} + \lambda_{y'}}{2}\right], \quad (1)$$

and

$$A_{minor} = \frac{\lambda_{x'} - \lambda_{y'}}{2\bar{\lambda}}, \quad (2)$$

where $\bar{\lambda}$ is the average of the eigenvalues (equivalent to averaged diffusivity $\overline{D}$), z' is the axis of greatest symmetry, and $\lambda_{x'}$ is greater than or equal to $\lambda_{y'}$. The parameter A_{major} ranges from -0.5 to 1.0, where the sign contains shape information. An A_{major} value that is greater than 0 indicates a prolate (''cigar-shaped'') diffusion ellipsoid where $\lambda_{z'}$ is the largest eigenvalue. An A_{major} value that is less than 0 indicates an oblate (''pancake-shaped'') diffusion ellipsoid where $\lambda_{z'}$ is the smallest eigenvalue. These measures may be useful but require that one solve for and sort the eigenvalues.

An alternative anisotropy measure is a coefficient of variation determined on the basis of the second moment (variance) of D (26):

$$A_\sigma = \frac{1}{\sqrt{6}\,\overline{D}} \times \sqrt{\sum_{i=x,y,z}(D_{ii} - \overline{D})^2 + 2(D_{xy}^2 + D_{xz}^2 + D_{yz}^2)}, \quad (3)$$

with $\overline{D}$ as already given. A_σ represents total anisotropy, irrespective of ellipsoid shape; it is on an absolute anisotropy scale and has a value between 0 and 1. A_σ is an invariant quantitative measure of anisotropy that does not require diagonalization of the diffusion tensor and is independent of the order of the eigenvalues. A_σ was derived to correspond in range and meaning to the spectroscopic definition of anisotropy used in the physical sciences (32). This is most easily seen in the axisymmetric approximation (26), where A_{minor} is 0, A_σ is the absolute value of A_{major} and

$$A_{major} = \frac{D_\parallel - D_\perp}{\overline{D}} = \frac{D_\parallel - D_\perp}{D_\parallel + 2D_\perp}, \quad (4)$$

with $D_\parallel = \lambda_{z'}$ and $D_\perp = \lambda_{x'} = \lambda_{y'}$. The parameter A_σ is similar to the relative anisotropy defined by Basser and Pierpaoli (28,29) except for a scaling factor of $2^{-1/2}$ contained in Equation 3 (also see factor of $2^{-1/2}$ in Eq [A1] in the Appendix) that places A_σ on an absolute anisotropy scale. A_σ also can be written in terms of A_{major} and A_{minor} (see Appendix, Eq [A2]).

The diffusion tensor is completely determined by measuring its six scalar components. This can also be viewed as sampling of sufficient points on the surface of the diffusion ellipsoid to constrain the ellipsoid size (ie, averaged diffusivity), shape (ie, A_{major}, A_{minor}), and orientation (ie, ϕ, θ, ψ). To reduce the effects of noise on the measurements, the diffusion ellipsoid should be sampled with strong gradients at points widely spaced over its surface while avoiding sampling of points related by inversion symmetry.

The tetrahedral gradient-encoding method (26) uses maximal simultaneous application of all three orthogonal gradients to construct each of the four noncolinear tetrahedral gradient vectors. This

method has an inherently high SNR for measurements of averaged diffusivity (18,30), because the tetrahedral gradients have a strength that is $3^{1/2}$ times larger than the orthogonal gradient-encoding method. Accordingly, the tetrahedral method also is expected to have favorable noise properties for A_σ measurement, particularly because of the wide uniform sampling of coordinate space (31). Linear combinations of the tetrahedral diffusion measurements D_1, D_2, D_3, and D_4 are used to evaluate the off-diagonal elements of the diffusion tensor (26). In cases of axisymmetric diffusion ($A_{minor} = 0$), these measurements describe the entire diffusion tensor. In more general cases, the individual diagonal elements of the diffusion tensor must be determined by means of additional sampling along other directions, such as the orthogonal x, y, and z magnet coordinate system. Combined tetrahedral-orthogonal encoding was chosen because the tetrahedral and orthogonal gradient vectors are complementary in terms of sampling of the diffusion tensor, since each set of vectors bisects the others to achieve wide coverage of the ellipsoid surface.

The diagonal element information is contained in the orthogonal gradient-encoded data, whereas the off-diagonal information is contained in the tetrahedral gradient-encoded data. Accordingly, A_σ as expressed in Equation (3) can be decomposed into two partial, noninvariant, anisotropy-weighted measures AW_{ortho} and AW_{tet}, which are dependent, respectively, on the orthogonal and tetrahedral measurements (see Appendix, Eqq [A4,A5]). The fractional amount of anisotropy contained in each of these measures can be expressed as $f_{tet} = AW_{tet}/A_\sigma$ and $f_{ortho} = AW_{ortho}/A_\sigma$ (see Appendix, Eqq [A7,A8]).

Data Acquisition

Approval for this study was obtained from the human studies committee at our institution. Quantitative diffusion-tensor MR imaging was performed in 13 neurologically healthy adults (11 men, two women; mean age, 31 years; age range, 23–47 years) recruited from the population at our institution. Informed consent was obtained from all subjects after the nature of the experiment was fully explained.

All examinations were performed with a 1.5-T system (Magnetom Vision; Siemens Medical Systems, Erlangen, Germany) equipped with a standard, circularly polarized clinical radio-frequency head coil. Custom single-shot spin-echo echo-planar MR pulse sequences with Stejskal-Tanner gradients were used. In each subject, diffusion-tensor information was collected by using a combination of tetrahedral (26) and orthogonal gradient-encoded diffusion-weighted images, together with reference signal intensity data. This tetrahedral-orthogonal configuration of diffusion-encoding directions was chosen because it was found to provide a high SNR for both averaged diffusivity and A_σ (simulations not shown). This configuration contains tetrahedral gradient vectors that are of maximal strength and spatial separation and three orthogonal vectors that bisect the tetrahedral vectors to provide sufficient measurements for overdetermined estimation of the full tensor, with wide angular coverage. Both angular coverage and gradient strength are important in anisotropy measurement (31). Other configurations for tensor measurement have been used, such as a three-dimensional hexagonal array (17,33,34), where all diffusion-weighted images can have the same diffusion-encoding strength (*b* factor) and echo time but where gradient strengths are weaker than those of tetrahedral encoding.

Quantitative diffusion-tensor data were acquired first under conditions optimized for accuracy for reporting of normative values. For this purpose, a peripherally gated single-section echo-planar MR imaging sequence (sequence A) was implemented with a nonselective 180° pulse and no cross terms. Axial MR images were acquired at the level of the basal ganglia in a subset of the subjects (nine men, two women; mean age 31 years; age range, 23–47 years). Each acquisition was repeated once under the same conditions to provide two identical data sets for noise calculation (35) and statistical testing (described later). Sequence A was used for measurement of all normative values reported herein.

To assess the performance of quantitative diffusion-tensor and anisotropy MR imaging under more clinically practical conditions, axial MR images were then acquired in six of the subjects (five men, one woman; mean age, 31 years; age range, 28–39 years) by using sequence B, a nongated multisection version of sequence A. Four of the six subjects (three men, one woman; mean age, 29 years; age range, 23–39 years) in the sequence B group underwent imaging with tetrahedral-only encoding and were also in the sequence A group. These data were used for statistical comparison between the single-section (sequence A) and multisection (sequence B) results. For the remaining two subjects (two men, aged 32 and 39 years) in the sequence B group, combined tetrahedral-orthogonal, whole-brain, multisection encoding was used. In one of these subjects, sequence B was used with additional repetitions to assess the effect of averaging of repeated image acquisitions.

For both sequences, the compensating lobes of the readout and phase-encoding gradients were applied after the diffusion-encoding gradients, and the section-selective gradient for the 90° radio-frequency pulse was refocused immediately to prevent cross terms between the diffusion and imaging gradients (31).

For sequence A, cross terms between the diffusion gradients and the imaging section–selective gradients were reduced further by using nonselective refocusing with a composite (one-two-one) 180° radio-frequency pulse. Thus, for sequence A, all phase shifts induced by imaging gradients were zero when the diffusion gradients were applied, and all cross terms with the diffusion gradients were zero. The composite nonselective 180° pulse was chosen to increase the uniformity of the 180° radio-frequency pulse, which potentially reduces the effect of radio-frequency inhomogeneities on diffusion encoding.

For sequence B, the only nonzero cross term was between the section-selective and the diffusion-encoding gradients, and this cross term (δ_{12}) contributed a diffusion coefficient error of less than 0.5% (31). For both sequences, navigator echo gradient pulses were present for all acquisitions, but the navigator echo of the reference image was used to correct all the diffusion-encoded acquisitions, because this procedure was found to reduce the severity of artifacts. The effect from the navigator echo gradient pulses and the readout and phase-encoding gradient pulses occurring during the echo-planar readout can contribute additional self and cross terms, but these are negligible in clinical echo-planar MR imaging (36).

When possible, diffusion-weighted MR images were acquired with a *b* value of approximately 1,000 sec/mm^2 in each encoding direction in conjunction with image data with a *b* value of approximately 0 sec/mm^2, to provide a high SNR per unit time (31,37). For the sequence A tetrahedral acquisitions, the input Cartesian gradients were 20.0 mT/m, and the echo time was 106 msec with a *b* value of 1,022 sec/mm^2 (diffusion-encoding durations δ of 17.0 msec and a time Δ between gradient onsets of 46.85 msec). For the orthogonal acquisitions, the echo time and the diffusion-encoding timings δ and Δ were lengthened to an echo time of 121

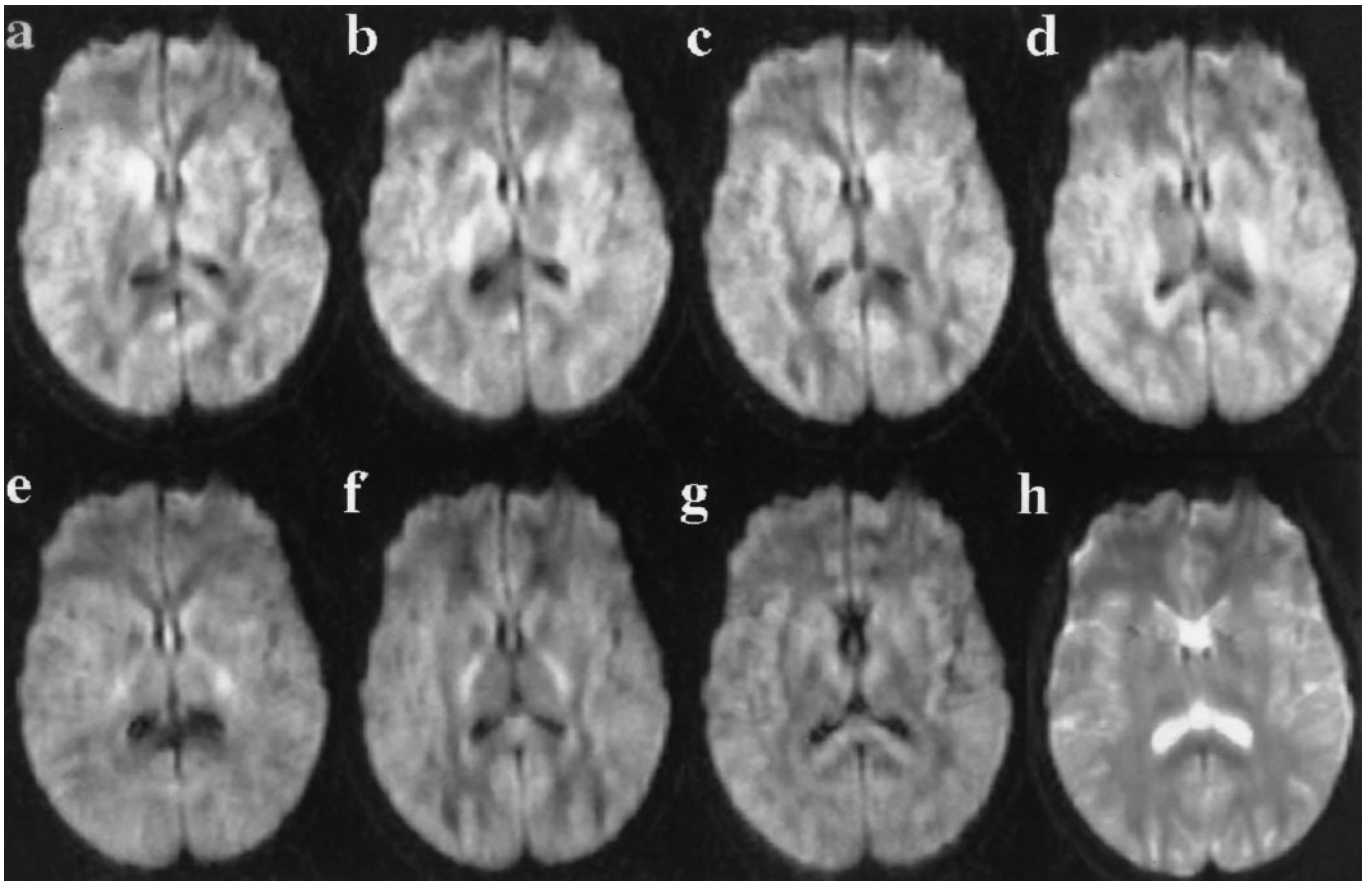

Figure 1. Characteristic axial single-section MR images (echo time = 106 msec, repetition time > 8,000 msec) obtained from a single acquisition of combined tetrahedral-orthogonal gradient encoding. *a–d,* Diffusion-weighted MR images encoded along tetrahedral directions one (*a*), two (*b*), three (*c*), and four (*d*) (26) by using a *b* value of 1,022 sec/mm^2. *e–g,* Diffusion-weighted MR images encoded along orthogonal directions x (*e*), y (*f*), and z (*g*) by using a *b* value of 999 sec/mm^2. *h,* One of the seven T2-weighted reference images acquired with very weak diffusion encoding ($b = 12$ sec/mm^2) for each encoding direction. Voxel sizes were 2.11 × 2.11 × 5.00 mm, and the imaging time was approximately 26 seconds per encoding direction (approximately 3 minutes total). All diffusion-weighted images are from a single acquisition and are displayed with the same window width and center, which are one-third the window width and center of *h*. Note the different WM contrasts in *a–g,* which encode anisotropic diffusion.

msec, δ of 27 msec, and Δ of 56.85 msec, to yield a *b* value of 999 sec/mm^2.

Data for each of the seven encoding directions were acquired with a separate pulse sequence, each with its own reference acquisition. Each reference acquisition had weak diffusion encoding ($b = 12$ sec/mm^2) along the same direction as the strong diffusion encoding, to spoil residual spurious free induction decay signals arising from imperfections in the nonselective 180° radio-frequency pulse. For sequence B, all diffusion-weighted images in the tetrahedral-only (four subjects) and tetrahedral-orthogonal (two subjects) cases were acquired with a combined pulse sequence that included one reference acquisition ($b = 0$ sec/mm^2). Weak diffusion encoding in the reference acquisition was found to be unnecessary in sequence B, because spurious free induction decay signals were reduced by means of the volume selectivity of the 180° radio-frequency pulse and the spoiling caused by the 180° section-selective gradient. For the tetrahedral-only sequence B case, the echo time, input gradient strength, and diffusion-weighted *b* factors were the same as those for sequence A. For the tetrahedral-orthogonal sequence B case, the input diffusion-encoding gradient strength was increased to 22.0 mT/m, and the echo time was reduced to 97 msec, which yielded a *b* value of 1,003.3 sec/mm^2 for tetrahedral encoding ($\delta = 15.75$ msec, $\Delta = 44.80$ msec). For the orthogonal encodings in this sequence, echo time and diffusion timings were the same as those in the tetrahedral encodings, with a *b* value of 334.3 sec/mm^2. The same timings were chosen for pulse sequence simplicity. Although this sequence has different diffusion-weighted *b* factors for tetrahedral and orthogonal encoding, this was not expected to contribute systematic error, on the basis of results from an initial study (not shown) that established that the same averaged diffusivity was measured with orthogonal encoding at *b* values of approximately 300 and 1,000 sec/mm^2.

In addition, for typical *b* factors and diffusion times used in clinical imaging, different groups (38,39) have found a lack of multiexponential dependence of brain signal intensity on the *b* factor, as well as a lack of explicit dependence of the brain diffusion coefficient on diffusion time at a constant *b* factor. Although multiple intravoxel tissue components can potentially lead to multiexponential dependence on the *b* factor, these results suggest that this effect is small, due possibly to the similarity in averaged diffusivity between gray matter (GM) and WM. Intravoxel averaging of multiple anisotropic components could lead to complex effects on diffusion-weighted images that are not completely described with one

tensor. Such partial volume effects were considered in simulations to be described subsequently.

To limit the effects of physiologic motion (eg, cerebrospinal fluid pulsatility), sequence A was gated so that the 90° pulse was applied 500 msec after the peak signal from the peripheral pulse oximeter, which corresponds to brain diastole (30,40). To reduce effects from heart rate variability in the presence of partial saturation of cerebrospinal fluid, the pulse sequence repetition time was set to a minimum of 8,000 msec. One warm-up step was programmed to ensure that cerebrospinal fluid signals were at steady state. The overall acquisition time was thus approximately 26 seconds to encode each direction with a small and a large *b* factor (approximately 3 minutes for one acquisition of all seven encoding directions).

Sequence B was performed with a repetition time of 3,050–3,500 msec without gating and with three warm-up steps. A 15-section axial set of tetrahedral-orthogonal brain data, including warm-up steps, was acquired in 33 seconds. This sequence was performed twice with gaps that were 100% of the section thickness, with the second acquisition offset by a section thickness. Thus, contiguous whole brain data were collected during 66 seconds, for an overall acquisition time of approximately 1½ minutes, including setup and tuning.

For qualitative assessment of the effectiveness of averaging acquisitions, three interleaved multisection data sets were acquired with 200% gaps in one subject, and these acquisitions were repeated to produce a total of 10 thin-section whole-brain data sets for averaging (total acquisition time, 16 minutes 40 seconds). For both sequences A and B, a sinusoidal readout gradient, a constant phase-encoding gradient, and linear time sampling were used to yield a raw data matrix of 96 × 200, which was interpolated to a rectilinear k-space matrix of 96 × 128 by using a gridding procedure. The field of view ranged from 180 × 240 mm to 210 × 280 mm (in-plane voxel size range, 1.88 × 1.88 mm to 2.19 × 2.19 mm). The section thickness was 5.0 mm in all cases except the triple-interleaved acquisition for sequence B, where the section thickness was 3.3 mm.

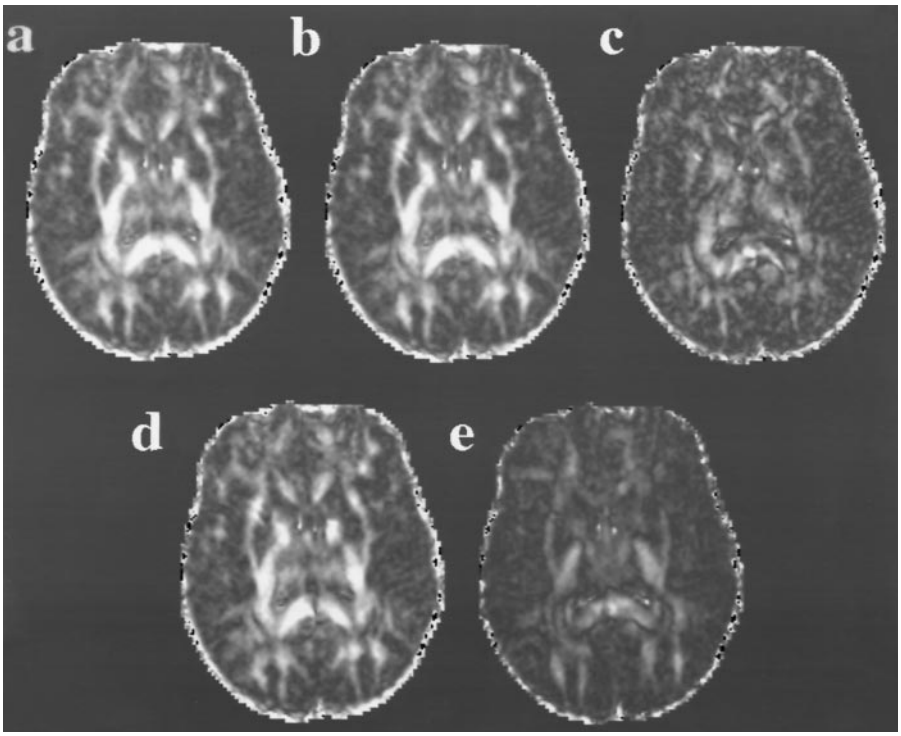

Figure 2. Axial anisotropy (*a–c*) and anisotropy-weighted (*d, e*) MR images computed at the level of the basal ganglia by using the data in Figure 1. A_σ (*a*), A_{major} (*b*), and A_{minor} (*c*) images were obtained from a single acquisition of combined tetrahedral-orthogonal encoding. *d*, AW_{tet} image was obtained from the tetrahedral encodings. *e*, AW_{ortho} image was obtained from the orthogonal encodings. All images have the same window width and center. Note the high sensitivity to WM depiction in *a*, with delineation of the external capsule, the peripheral occipital WM projections, the thalamic heterogeneity, and the width of the internal capsule. Note also the structural heterogeneity of WM in *a* (eg, dark bands between the internal capsule, corpus callosum, and adjacent WM) and the heterogeneity in the thalamus, which is not seen on T2-weighted MR images (see Fig 1, *h*). Visible differences in anisotropy strength exist between WM classes, where the image intensity in *a* and *b* can be ranked, from highest to lowest, as follows: commissural WM, projection WM, and association WM. In comparison with *a*, the anisotropy-weighted component images in *d* and *e* show a loss of intensity in the splenium and genu of the corpus callosum, respectively, and there generally is less intensity in *e*, as compared with that in *d*.

Data Analysis

Images were sinc interpolated to a 192 × 256 image matrix (0.94 × 0.94 × 5.00 mm pixels in sequence A) to facilitate selection of ROIs. In some cases, the rectilinear matrix produced after k-space gridding was zero filled prior to reconstruction; in the other cases, the interpolation was performed after reconstruction.

All images were realigned in two dimensions to the reference images to correct for two-dimensional displacements and linear distortions (ie, stretch and shear) caused by eddy currents. These linear distortions have been found to constitute the major eddy-current effects in echo-planar diffusion MR imaging (41), which also was supported by cine visual inspection of the realigned images in the present study. The realignment algorithm used a combination of intramodality (42) and cross-modality affine realignment procedures; the cross-modality procedure was used for realignment of image pairs with substantial contrast differences. We routinely use these intra- and cross-modality realignment procedures for functional MR imaging (43). Because all realignments were to the reference echo-planar MR image, the realignment was specifically targeted to low-order eddy-current–induced distortions, which must be corrected to bring the reference and diffusion-weighted images into register for tensor computation (described subsequently). Higher-order distortions also were typically present on the echo-planar MR images (in comparison with those on anatomic spin-echo MR images), but these need not necessarily be corrected for the diffusion computation because the distortions are constant on all diffusion-weighted and reference images. Eddy-current effects also were specifically targeted by performing the realignments in two dimensions, because the principal eddy-current effects are in plane. The realignment procedure additionally corrects for in-plane subject motion, although typical in-plane and through-plane motion effects are estimated to be very small in comparison with the eddy-current effects at these acquisition times.

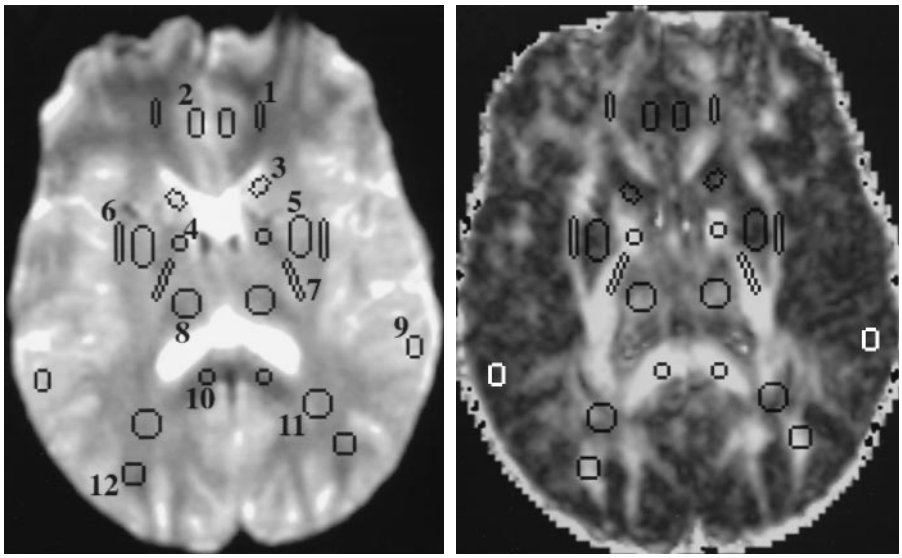

a. **b.**

Figure 3. ROIs used in data analysis are superimposed on **(a)** axial T2-weighted reference MR image (echo time = 106 msec, repetition time > 8,000 msec) (same image as Fig 1, *h*) and **(b)** axial A_σ MR image (same image as Fig 2, *a*). *1* = frontal WM, *2* = frontal GM, *3* = head of the caudate nucleus, *4* = genu of the internal capsule, *5* = putamen, *6* = external capsule, *7* = posterior limb of internal capsule, *8* = thalamus, *9* = occipital-temporal GM, *10* = splenium of the corpus callosum, *11* = occipital WM, and *12* = optic radiations. The location of the ROI for occipital-temporal GM varied across subjects. ROI sizes and shapes were kept constant across hemispheres but varied across subjects.

Tetrahedral and orthogonal diffusion-weighted images were obtained. The intensities are functions of the *b* factors and the elements of the diffusion tensor, weighted by the direction of the diffusion gradient used (27,31). The logarithm of these intensities was computed to create a set of linear equations that were solved by using standard weighted least-squares techniques (13,14,44). The six diffusion tensor elements were determined with global analysis (see Appendix) of all eight tetrahedral-orthogonal log intensities, and averaged diffusivity $\overline{D}$ and A_σ were then computed directly from the diffusion-tensor elements according to Equation (3) (see Appendix, Eq [A1]). Images were computed on a pixel-by-pixel basis, without spatial filtering.

From the estimated diffusion tensor, the principal axes and eigenvalues were then computed by using standard matrix procedures. The eigenvalues were sorted according to size and symmetry ($\lambda_{z'} > \lambda_{x'} > \lambda_{y'}$ for the prolate case, $\lambda_{x'} > \lambda_{y'} > \lambda_{z'}$ for the oblate case), and A_{major} and A_{minor} were calculated by using Equations (1,2). In addition, by using only the tetrahedral or orthogonal data, anisotropy-weighted images were calculated (see Appendix, Eqq [A4,A5]) by means of direct computation of D_1, D_2, D_3, and D_4, or D_{xx}, D_{yy}, and D_{zz}, from log intensity ratios. In the one sequence B case where the acquisition was repeated multiple times for the purpose of averaging, the diffusion-weighted images and reference image were arithmetically averaged prior to the log intensity computation. Averaging was performed at this stage, as opposed to averaging of computed A_σ images, to minimize anisotropy bias caused by input noise (discussed subsequently). The fraction of total anisotropy contained in the anisotropy-weighted measures also was computed for arbitrary orientations and was displayed with MATLAB software (MathWorks, Natick, Mass) by using Equations (A7,A8) in the Appendix.

Elliptical ROIs were positioned on each subject data set by using interactive software (ANALYZE; Mayo Foundation, Rochester, Minn) for evaluation of anisotropy in different anatomic areas of the brain. The ROI calculations were performed by using a custom program that partially weights edge voxels according to the fraction of the voxel that lies inside the ROI, as determined with analytic ellipse expressions. This procedure was performed instead of more standard routines that sample only voxels that are completely inside the ROI. This procedure is equivalent to obtaining ROI measurements on highly interpolated images (but without large memory or disk requirements).

Normative data were measured from ROIs of 12 brain regions in the 11 subjects examined with sequence A. The ROIs were placed in equivalent structures in each hemisphere for averaging and analysis of hemispheric differences. In each subject, the ROIs were initially located by using the T2-weighted reference images (echo time = 106 msec, repetition time > 8,000 msec), and ROI sizes and positions were refined by means of overlay onto the A_σ images. Mean ROI values were measured for all 12 regions in each hemisphere, for each of the two acquisitions, and for each subject. Statistical variations across these factors were assessed with the two-tailed Student *t* test of the mean ROI values. The random (thermal) noise properties of images also were estimated in individual subjects by subtracting the two images acquired under identical experimental conditions (35). The thermal noise of a single acquisition was taken as $2^{-1/2}$ times the single-pixel SD measured from the subtraction image by using the ROIs. The SNR was estimated as the mean of the two acquisitions divided by the thermal noise value. The subtraction images were also inspected visually for artifacts, especially in the locations of the ROIs. No ROI positions were changed, and all data were included in the measurements and statistical analyses.

Computer Simulations

Computer simulations were performed to evaluate the effects of noise and partial volume averaging on the measurement of anisotropy. In a noise-free isotropic region, the true A_σ is 0. In the presence of noise, the measured A_σ is greater than 0 even in isotropic regions, because, according to Equation (3), noise causes variance in the diffusion measurements that elevates A_σ. This low-level anisotropy is expected to be strongly dependent on the SNR of the measurement.

To evaluate the baseline isotropic level of A_σ at different noise levels, a Monte Carlo program was written that generated voxel intensity data for an idealized tissue having the same averaged diffusivity as the brain ROI under consideration but with the assumption of zero anisotropy ($A_\sigma = 0$). The signal intensities that would be observed in isotropic tissues in a tetrahedral-orthogonal diffusion experiment were simulated by calculating the ideal signal intensity and adding Gaussian random noise. The ideal signal intensity was calculated by assuming (*a*) that *b* equalled 1,000 sec/mm^2 for all seven diffusion-weighted images and (*b*) that all diffusion-weighted images and the reference T2-weighted image had the same echo time.

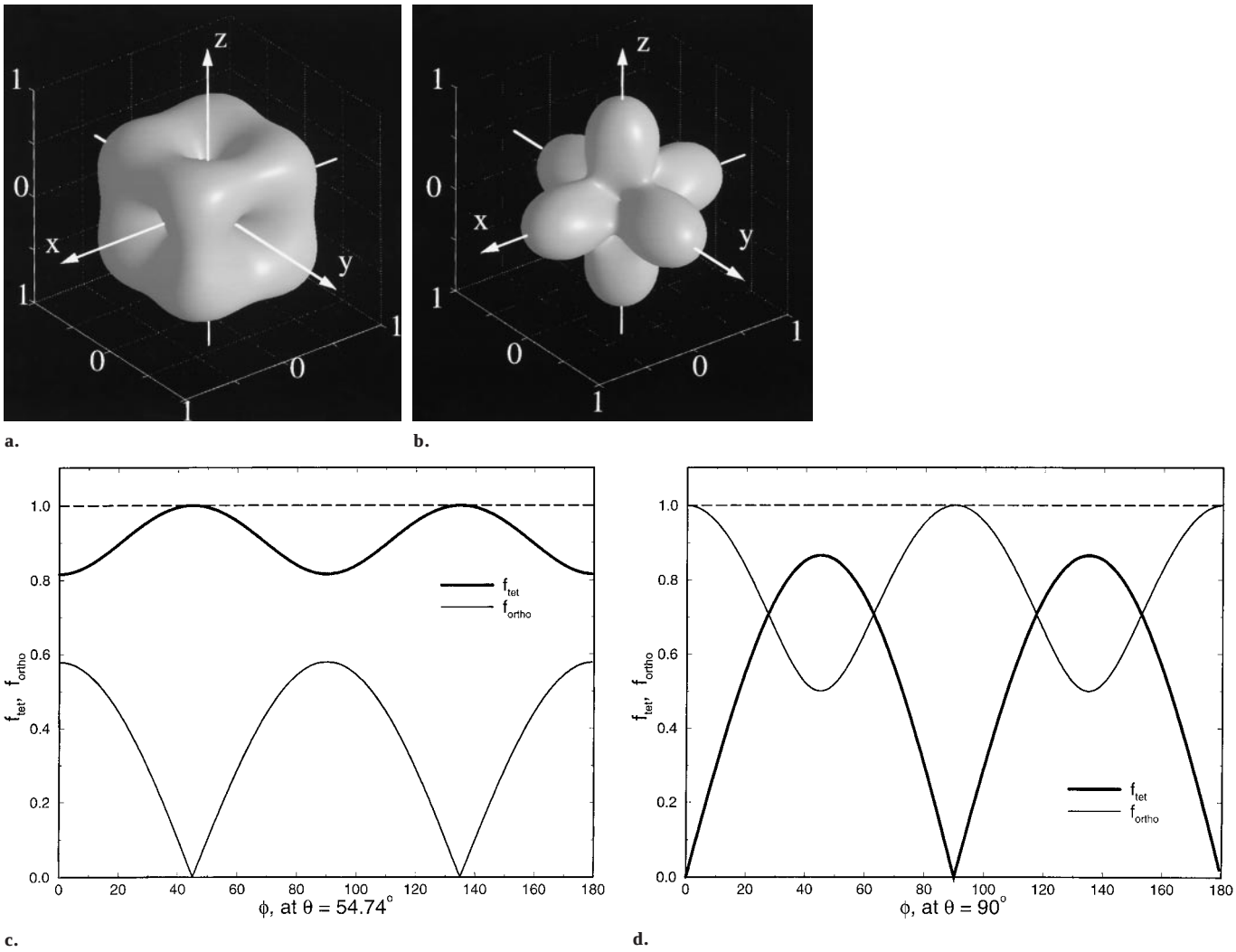

Figure 4. Ratio of tetrahedral and orthogonal anisotropy-weighted indexes (AW_{tet} and AW_{ortho}) to total anisotropy (A_σ) as a function of θ and ϕ. Three-dimensional displays of the ratios **(a)** f_{tet} and **(b)** f_{ortho} were computed by using Equations (A7) and (A8) (see Appendix), respectively. These ratios are displayed as the radial distance of a surface in a spherical coordinate system as a function of the directional angles θ and ϕ. **(c, d)** Graphs that show profiles of the data when **(c)** θ is 54.74° and **(d)** θ is 90° indicate the orientation of the maxima and minima. The recovery of A_σ generally is higher for the AW_{tet} measurement than for the AW_{ortho} measurement. Thus, the majority of the anisotropy information is in the tetrahedral measurements (ie, the majority of anisotropy information is contained in the off-diagonal tensor elements). Note the extent to which the surfaces in **a** and **b** approach the ideal case of a sphere (ie, a true A_σ measurement, also indicated by the approach of the solid curves to the dashed lines in **c** and **d**). Note also that the surfaces in **a** and **b** are complementary, with AW_{tet} insensitive in the orthogonal directions and AW_{ortho} insensitive in the tetrahedral directions.

Gaussian noise was added to real and imaginary channels at various reference image SNR levels. A constant level of uncorrelated noise was assumed for the diffusion-weighted and reference images. The A_σ value was calculated from these simulated intensities by using Equation (3), and A_σ statistics were determined from 16,000 sets of simulated tetrahedral-orthogonal diffusion experiments. The mean and SD of the computed A_σ values were compared with the experimentally determined, average ROI A_σ value within subjects.

The second simulation was performed to evaluate the effect of partial volume averaging on the measurement of A_σ. This is especially important in transition zones between regions of high anisotropy and those of low anisotropy, such as the borders between GM and WM and in areas of WM with fibers that cross in different directions. Anisotropy measurements in voxels located at GM-WM interfaces were simulated by assuming a mixture of idealized WM and GM tissue components on the basis of ROI measurements in homogeneous areas of GM and WM. The WM tissue component was modeled to have the same $\overline{D}$ and A_σ values as the splenium of the corpus callosum ($\overline{D} = 0.72 \times 10^{-3}$ mm²/sec, A_σ = 0.5), but with zero minor-axis anisotropy ($A_{minor} = 0$) to represent an idealized axisymmetric case imaged at high spatial resolution. The GM component was chosen to be representative of the putamen ($\overline{D} = 0.72 \times 10^{-3}$ mm²/sec), but with zero anisotropy ($A_\sigma = 0$). Noise-free signal intensities were calculated separately for GM and WM and were combined at various partial volume weightings, from which A_σ was calculated by using Equation (3).

In the third simulation, we evaluated the case of WM regions with crossing fibers. Anisotropy measurements were simulated for WM tracts that crossed at variable angular separations within the

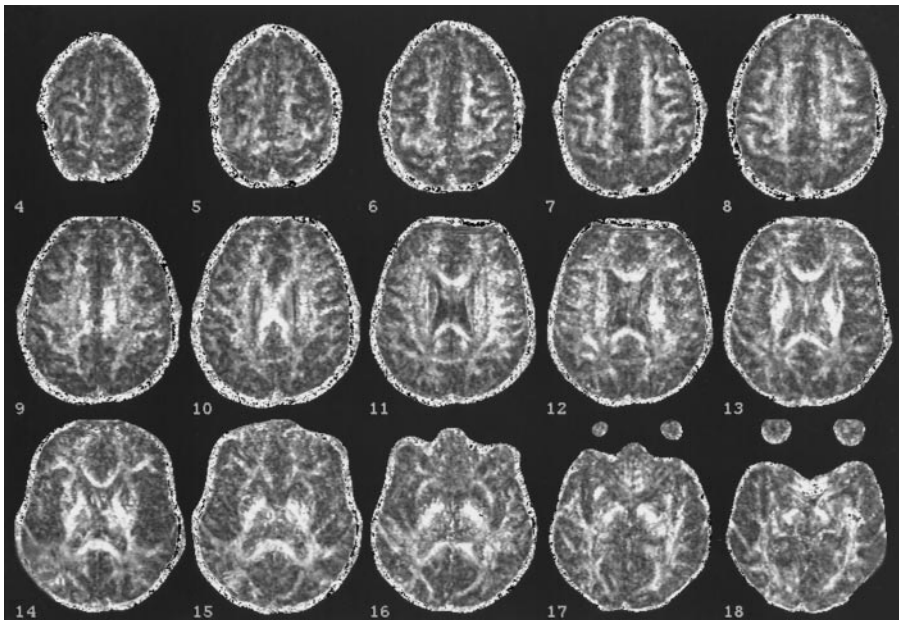

a.

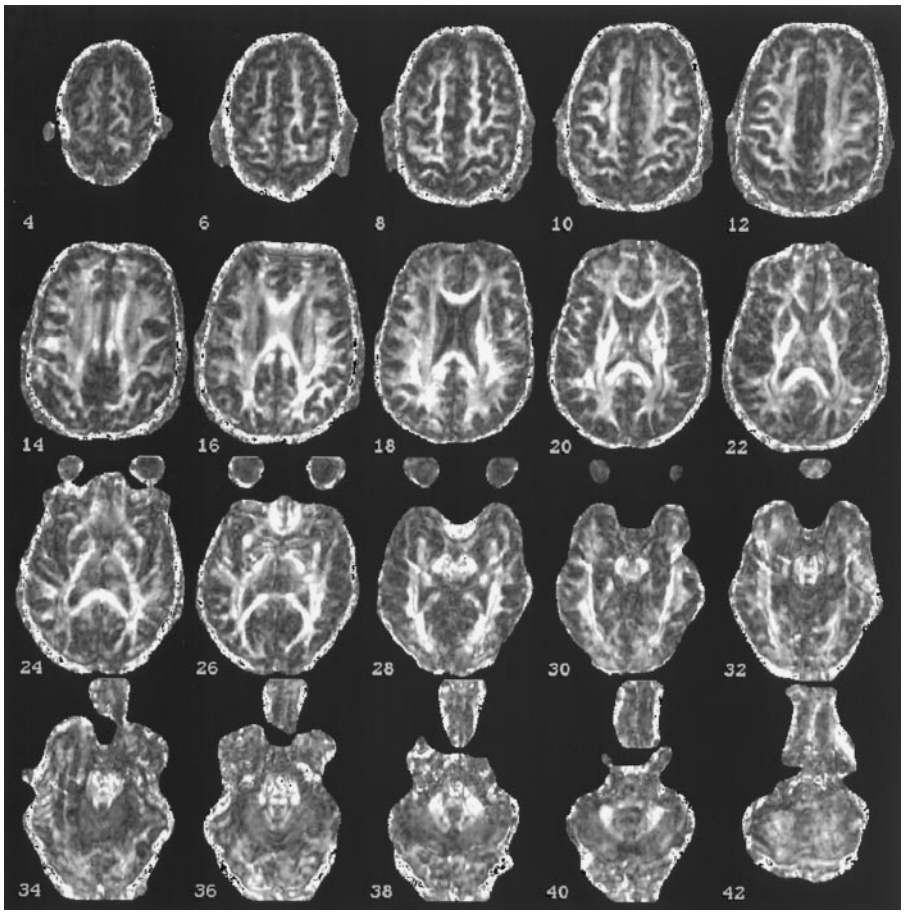

b.

Figure 5. Axial multisection MR imaging demonstration of A_σ obtained **(a)** without and **(b)** with data averaging. Numbers indicate the section numbers. Combined tetrahedral-orthogonal multisection data were acquired with one axial T2-weighted reference MR image obtained with a single sequence (echo time = 97 msec, repetition time = 3,100 msec), with *b* of 1,003.3 sec/mm^2 for tetrahedral data, *b* of 334.4 sec/mm^2 for orthogonal data, and *b* of 0 sec/mm^2 for reference data. In **a,** only one image was acquired per encoding direction (one shot per image; total acquisition time, 66 seconds), with a voxel size of 1.88 × 1.88 × 5.00 mm. In **b,** the pulse sequence used in **a** was repeated a total of 10 times in a different subject (total acquisition time, 16 minutes 40 seconds) but with a section thickness of 3.3 mm. In **b,** the source image data as depicted in Figure 1 were averaged, followed by computation of the diffusion tensor. In both **a** and **b,** A_σ was computed from the estimated diffusion tensor according to Equation (3). Note the sensitive demonstration of WM structures throughout the brain, including subcortical U fibers. In addition to the findings shown in Figure 2, note the detection of other WM structures such as cerebral peduncles (section *18* in **a** and section *30* in **b**) and the cerebellar peduncles (sections *38* and *40* in **b**), as well as heterogeneity in the thalamus, basal ganglia, and occipital WM (eg, in **b,** note band of anisotropy in the region of the globus pallidus in sections *24* and *26* and ridges of low anisotropy along the optic radiations in sections *20–32*). Comparison of **a** and **b** indicates that A_σ image quality can be improved by increasing the number of signals acquired and obtaining thinner sections.

plane of a transverse image. Signal intensities were calculated for two tissue components, each modeled as for the idealized WM tissue in the second simulation and each containing fibers oriented in the plane ($\theta = 90°$). The signals were added at equal weightings for varying in-plane angles (one component with $\phi = 0°$, the other with $-90° < \phi \leq +90°$). The A_σ value of the combined voxel was calculated with Equation (3) and compared with the two component values.

RESULTS

Figure 1 presents a complete set of characteristic single-section diffusion-weighted MR images obtained from one of the subjects (sequence A): four tetrahedral diffusion-weighted images (Fig 1, *a–d*), three orthogonal diffusion-weighted images (Fig 1, *e–g*), and the baseline T2-weighted reference image (Fig 1, *h*). Different levels of brightness in the diffusion-weighted images are due to the anisotropy of WM fiber tracts that were sampled along different directions.

Figure 2 presents the anisotropy images computed from the data in Figure 1. Images of the various anisotropy measures have a wide range of intensities in the brain, in contrast to the typically uniform appearance of the adult brain on averaged diffusivity images (17,18). Areas of high A_σ in Figure 2, *a,* are seen in the corpus callosum, internal capsule, and

TABLE 1
Mean Anisotropy Measures from Brain ROIs in 11 Human Subjects: Single-Section Data

ROI	A_σ	A_{major}	A_{minor}	AW_{tet}	AW_{ortho}	RA/$2^{1/2}$*
Commissural WM						
Splenium of corpus callosum	0.50 (0.02)	0.49 (0.02)	0.16 (0.01)	0.45 (0.01)	0.21 (0.02)	0.46 (0.02)
Projection WM						
Genu of internal capsule	0.45 (0.02)	0.43 (0.02)	0.21 (0.01)	0.44 (0.02)	0.07 (0.01)	0.37 (0.01)
Posterior limb of internal capsule	0.39 (0.02)	0.38 (0.02)	0.13 (0.01)	0.30 (0.02)	0.24 (0.01)	0.42 (0.02)
Optic radiations	0.31 (0.02)	0.30 (0.02)	0.13 (0.01)	0.29 (0.02)	0.11 (0.01)	No data
Association WM						
Frontal WM	0.26 (0.01)	0.23 (0.01)	0.18 (0.02)	0.22 (0.02)	0.12 (0.01)	0.22 (0.02)
External capsule	0.23 (0.02)	0.21 (0.02)	0.13 (0.01)	0.21 (0.02)	0.08 (0.01)	No data
Occipital WM	0.21 (0.01)	0.19 (0.01)	0.12 (0.01)	0.16 (0.01)	0.11 (0.01)	No data
Thalamus	0.19 (0.01)	0.16 (0.01)	0.15 (0.01)	0.17 (0.01)	0.05 (0.005)	No data
GM						
Head of caudate nucleus	0.10 (0.01)	0.09 (0.01)	0.08 (0.005)	0.09 (0.01)	0.04 (0.01)	0.11 (0.004)
Frontal GM	0.09 (0.01)	0.08 (0.01)	0.07 (0.01)	0.08 (0.01)	0.04 (0.01)	No data
Putamen	0.08 (0.01)	0.07 (0.01)	0.07 (0.004)	0.07 (0.01)	0.03 (0.003)	0.11 (0.01)
Occipital-temporal GM	0.05 (0.003)	0.05 (0.003)	0.04 (0.003)	0.05 (0.003)	0.02 (0.002)	0.13 (0.01)

Note.—Data based on computed anisotropy and anisotropy-weighted MR images obtained with sequence A (single-section method; Fig 2). Means are derived from ROI measurements (Fig 3) of both hemispheres from two equivalent sections, averaged across subjects, and weighted by the ROI area. Number in parentheses is the SEM weighted by ROI area, unless otherwise noted. SEM was calculated as SD of mean values from each subject, divided by the square root of the number of subjects.

* Data are results in six monkeys reported by Pierpaoli and Basser (29) expressed in terms of A_σ. Number in parentheses is the SEM. RA = relative anisotropy.

optic radiations. The external capsule also is well depicted. The ROIs were located on the reference image and were confirmed with A_σ images, as shown in Figure 3. Comparison of A_σ values between the matched left and right ROIs demonstrated no statistically significant differences on the basis of measured within-subject thermal noise levels and the results of a two-tailed pairwise Student *t* test at the 95% confidence level. Comparison of A_σ ROIs between the first and second acquisition in each volunteer similarly demonstrated no significant differences from thermal noise at the 95% confidence level.

Figure 2, *b* and *c*, are images of A_{major} and A_{minor}, respectively. A_{major} and A_σ are similar in appearance and, when diffusion is axisymmetric, equal in magnitude. Figure 2, *d* and *e*, are images of AW_{tet} and AW_{ortho}, respectively. In general, the intensity of AW_{tet} is larger than that of AW_{ortho}. Artifactual loss of intensity is seen in AW_{tet} in the midline of the splenium of the corpus callosum and in AW_{ortho} in the genu of the corpus callosum owing to fiber direction. The fraction of anisotropy recovered by separate tetrahedral and orthogonal anisotropy-weighted indexes is displayed in Figure 4 for different orientations by using Equations (A7,A8), in the Appendix.

Figure 5a presents A_σ in the 66-second multisection experiment (sequence B). Comparison of ROI A_σ values between single-section and multisection acquisitions at the same level demonstrated no significant differences within subjects on the basis of measured thermal noise and the results of a two-tailed pairwise Student *t* test at the 95% confidence level. Figure 5b demonstrates the ability to average A_σ. These data were acquired as an average of 10 66-second multisection acquisitions. In Figure 5, high anisotropy is present in WM tracts throughout the brain, such as the centrum semiovale, the subcortical U fibers, and the cerebral and cerebellar peduncles.

Table 1 presents values for several anisotropy measures in the brain ROIs demonstrated in Figure 3. These include A_σ, A_{major}, and A_{minor}, as in Figure 2, *a–c*. The ROIs are sorted in order of decreasing A_σ value and demonstrate the variability of anisotropy between different types of WM and GM. Additional columns in Table 1 show the comparison of A_σ with its noninvariant components and with AW_{tet} and AW_{ortho}, which were obtained separately by using the tetrahedral and orthogonal techniques, respectively. The larger anisotropy contribution contained in the tetrahedral component as compared with that in the orthogonal measure is again demonstrated. Also, our human A_σ results are compared with the relative anisotropy

TABLE 2
Mean Principal Diffusion Coefficients (Eigenvalues) for Various ROIs

ROI	$\lambda_{z'}$	$\lambda_{x'}$	$\lambda_{y'}$
Commissural WM			
Splenium of corpus callosum	1.43 (0.08)	0.49 (0.04)	0.25 (0.03)
Projection WM			
Genu of internal capsule	1.33 (0.05)	0.57 (0.04)	0.26 (0.03)
Posterior limb of internal capsule	1.23 (0.05)	0.52 (0.03)	0.34 (0.02)
Optic radiations	1.18 (0.06)	0.61 (0.03)	0.43 (0.03)
Association WM			
Frontal WM	1.17 (0.06)	0.75 (0.03)	0.47 (0.03)
External capsule	1.14 (0.05)	0.73 (0.04)	0.52 (0.03)
Occipital WM	1.07 (0.04)	0.73 (0.03)	0.54 (0.03)
Thalamus	0.94 (0.04)	0.72 (0.03)	0.50 (0.03)
GM			
Head of caudate nucleus	0.94 (0.03)	0.79 (0.02)	0.66 (0.03)
Frontal GM	1.02 (0.04)	0.88 (0.03)	0.75 (0.03)
Putamen	0.84 (0.03)	0.73 (0.02)	0.63 (0.02)
Occipital-temporal GM	1.02 (0.04)	0.93 (0.04)	0.85 (0.04)

Note.—ROI data were measured on the basis of eigenvalue images computed from single-section (sequence A) source images shown in Figure 1. Number in parentheses is the SEM, which was calculated as for Table 1.

TABLE 3
Comparison of Differences among A_σ Values in Various Brain ROIs

	ROI											
ROI	CCS	ICG	ICP	OR	FWM	EC	OWM	Th	HC	FGM	Pu	OTGM
CCS		T	T									
ICG	T		T	T								
ICP	T	T		T	T							
OR		T	T		T	T	T	T				
FWM			T	T		T	T	T				
EC				T	T		T	T				
OWM				T	T	T		T				
Th				T	T	T	T					
HC										T	T	
FGM									T		T	T
Pu									T	T		T
OTGM										T	T	

Note.—CCS = splenium of corpus callosum, EC = external capsule, FGM = frontal GM, FWM = frontal WM, HC = head of caudate nucleus, ICG = genu of internal capsule, ICP = posterior limb of internal capsule, OR = optic radiations, OTGM = occipital-temporal GM, OWM = occipital WM, Pu = putamen, T = ''true'' null hypothesis (A_σ values not significantly different, per student *t* test and 95% confidence level), Th = thalamus.

divided by $2^{1/2}$, as evaluated in monkeys by Pierpaoli and Basser (29). This comparison was made because relative anisotropy is the anisotropy measure mentioned in the MR imaging literature that is most closely related to A_σ. There is general agreement between A_σ and relative anisotropy divided by $2^{1/2}$. The A_σ SNR averaged across subjects in the reported WM structures ranged from 5.1 to 15.6. The measured thermal noise levels in A_σ, A_{major} and A_{minor} (0.0118, 0.0112, and 0.0121, respectively) were similar to one another.

Table 2 presents characteristic values of sorted eigenvalues obtained from the same ROIs as those in Table 1. Table 3 presents results of the pairwise Student *t* test comparison of A_σ between different ROIs. The null hypothesis was that there is no significant difference in A_σ between ROIs at the 95% confidence level. Table 3 indicates ROI comparisons for which the null hypothesis was true, that is, ROIs that were not significantly different from each other at the 95% confidence level. If anisotropy were uniform across the brain, the null hypothesis would have been true for all comparisons. If all ROIs differed from one another, only the diagonal elements of Table 3 would have been filled. The actual results in Table 3 resemble a block-diagonal structure, in which A_σ is significantly similar within tissue groups (ie, blocks) and significantly different across groups.

The simulation results for noise and partial volume effects on measurement of A_σ are given in Figures 6 and 7, respectively. In Figure 6a, the measurement bias in the A_σ of isotropic tissues caused by noise is graphed versus the SNR on the reference T2-weighted image for tetrahedral-orthogonal encoding with a *b* value of 1,000 sec/mm^2 for all encodings. The results of this simulation demonstrate that the values measured in GM and the basal ganglia are consistent with zero anisotropy ($A_\sigma = 0$) at the reference T2-weighted SNR levels present in the experiment (reference SNR of approximately 40–60).

In Figure 6b, the A_σ measurement bias is graphed versus true anisotropy for anisotropic tissues at various SNR levels for the same tetrahedral-orthogonal encoding. The results of this simulation demonstrate that the anisotropy values measured in the thalamus ($A_\sigma = 0.19$) and in other WM areas in Table 1 are consistent with an A_σ value that is greater than 0 at the experimental SNR levels. The results of this simulation also indicate that the noise in A_σ was not stationary but instead increased as A_σ increased (see error bars in Fig 6b).

A simulation of the partial volume effects on A_σ in border regions between GM and WM is presented in Figure 7a. The results of this simulation demonstrate that a combination of signals from anisotropic and isotropic diffusion elements within a voxel generally caused reduction in the measured A_σ proportional to the relative amount of isotropic tissue (given the assumption that the components have similar T1 and T2 weightings). The partial volume effects of averaging between two groups of WM fibers with equal anisotropy is simulated in Figure 7b as a function of angular separation. In this case, the measured A_σ value was reduced by an amount that was dependent on the degree of angular separation between the component tensors.

DISCUSSION

Quantitative images of different anisotropy measures were obtained by means of a combination of measurements with tetrahedral and orthogonal gradient encoding (Figs 2, 5). This combination provides wide spatial coverage of the diffusion ellipsoid surface at high gradient strength. The tetrahedral encodings represent the most widely spaced set of four encoding directions (and are at the maximum gradient strength), whereas the orthogonal encodings are in directions that bisect the angular gaps of the tetrahedral encodings. The invariant anisotropy measure A_σ has multiple advantages, including an absolute anisotropy scale and direct calculation from the diffusion-tensor elements without matrix diagonalization or eigenvalue sorting.

The A_σ MR images shown in Figure 2, *a*, and Figure 5 demonstrate anatomic detail that is not typically evident on conventional T1- and T2-weighted MR images. This detail includes depiction of the peripheral extensions of the densely myelinated optic radiation and the posterior limb of the internal capsule. In particular, the posterior limb of the internal capsule appeared wider on A_σ MR images than on conventional MR images, which is compatible with the appearance on gross anatomic sections (eg, see figs 8 and 13 in DeArmond et al [45]). The anterior limb of the internal capsule appeared thinner than the posterior limb and tapered anteriorly, which again is compatible with the appearance on gross anatomic sections (figs 13 and 14 in DeArmond et al). As a consequence, ROI measurements are not reported for the anterior limb of the internal

capsule, because this structure was too thin to yield reliable results. The thin external capsule was well defined, which helped demarcate the lateral extent of the putamen.

Strong anisotropy also was present in the centrum semiovale, the peripheral U fibers, and the cerebral and cerebellar peduncles. The anisotropy MR images provided evidence for substructures in the thalamus and in the occipital WM, which otherwise appear homogeneous on conventional T1- and T2-weighted MR images. This high sensitivity to WM structure presumably is due to suppression of adjacent GM, which has zero anisotropy (confirmed by the simulation results shown in Fig 6a), and to the straightforward, nearly linear partial volume effects at GM-WM interfaces (confirmed by the simulation results in Fig 7a). This phenomenon is similar to the improvement of small vessel detection in MR angiography due to suppression of the signal from adjacent tissue.

Signal averaging was effective at improving the sensitivity to WM structures, as seen by comparing Figure 5a with Figure 5b. Figure 5 also demonstrates other regions of structural heterogeneity in WM, such as the ''ridged'' appearance of decreased anisotropy adjacent to the optic radiations and splenium of the corpus callosum on sections 20 and 22 in Figure 5b. The simulation results shown in Figure 7b indicate that partial volume averaging between WM fiber tracts can lead to a decrease of more than 50% in measured anisotropy, which may be a possible cause of this appearance. Another example is heterogeneity in the basal ganglia, seen in the region of the globus pallidus, which may be due to structures such as the ansa lenticularis (section 24 in Fig 5b). Further investigation is needed to assess the relevance of these findings for clinical anisotropy MR imaging.

The results in Tables 1 and 2 indicate that consistent A_σ values and principal diffusion coefficients can be measured across subjects for different brain regions, as indicated by the small SEMs in Tables 1 and 2. This consistency across subjects indicates that there generally are characteristic values for A_σ in different brain structures in healthy adults. The results also indicate that there are significant differences in A_σ across brain regions, as was also found by Pierpaoli and colleagues (17,29). The general correspondence between A_σ in humans and relative anisotropy divided by $2^{1/2}$ in monkeys (29) also is suggestive that these characteristics may extend across species. The consistency of data across human subjects

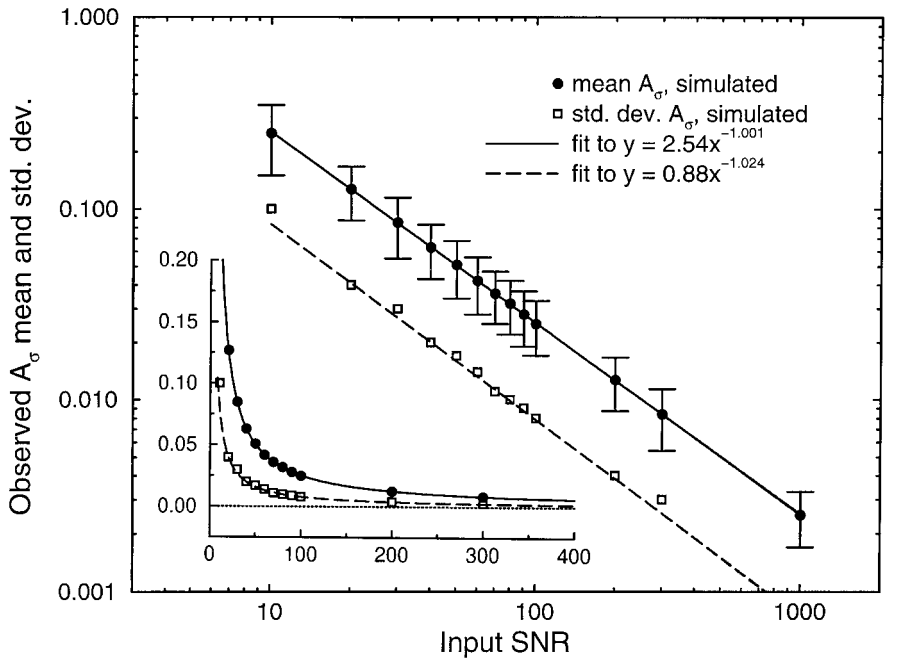

a.

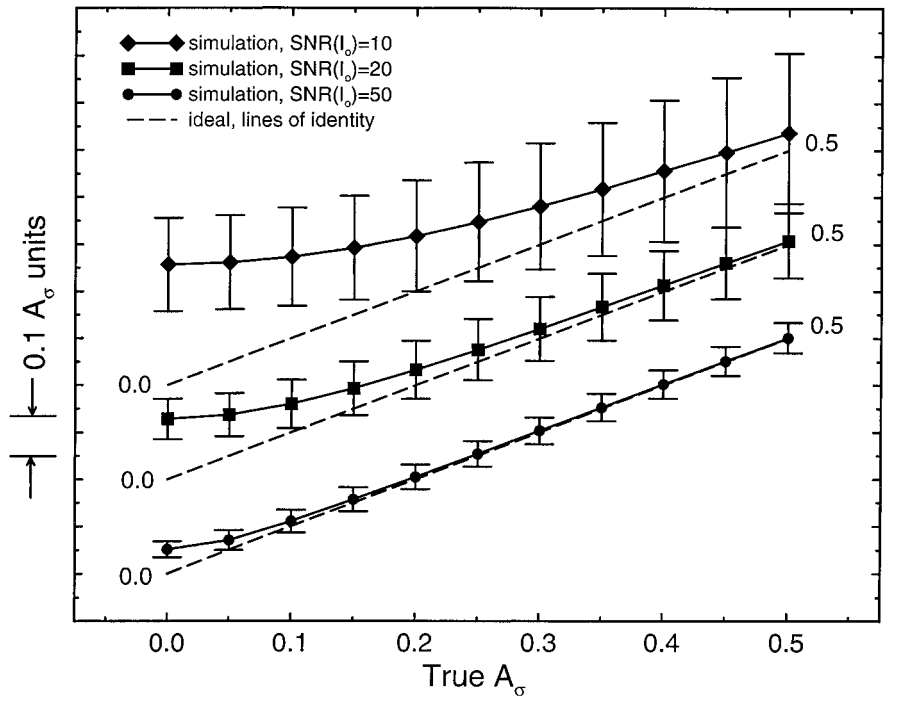

b.

Figure 6. Graphs show results of simulation of the effect of noise on the accuracy and precision of A_σ measurements for **(a)** isotropic tissues and **(b)** axisymmetric anisotropic tissues. **(a)** Bias and random noise in the observed A_σ are graphed on linear (inset) and log-log scales versus the input SNR on the T2-weighted reference image. The bias and random noise are calculated as the mean and SD (*std. dev.*) of multiple experimental simulations as described in Materials and Methods. The simulation in **a** is for an ideal isotropic GM tissue that has the averaged diffusivity value of the putamen ($\overline{D} = 0.72 \times 10^{-3}$ mm^2/sec). The mean and SD in A_σ are fit to the expression $y = Ax^B$, where A is the value at an SNR of 1 and B is the power of the dependence on SNR. **(b)** Bias and random noise in the observed A_σ are graphed as a function of A_σ at different reference image (I_0) SNR levels for an ideal axisymmetric WM tissue that has the same averaged diffusivity value as in **a,** similar to the averaged diffusivity value of the splenium of the corpus callosum. The simulations are for an A_σ value that ranges from 0.0 to 0.5, to represent the range for tissues shown in Table 1. Three reference SNR levels indicative of a range of MR imaging hardware are simulated, and the results are offset on the vertical axis for clarity. The SNR for the data acquired for Table 1 was approximately 40–60.

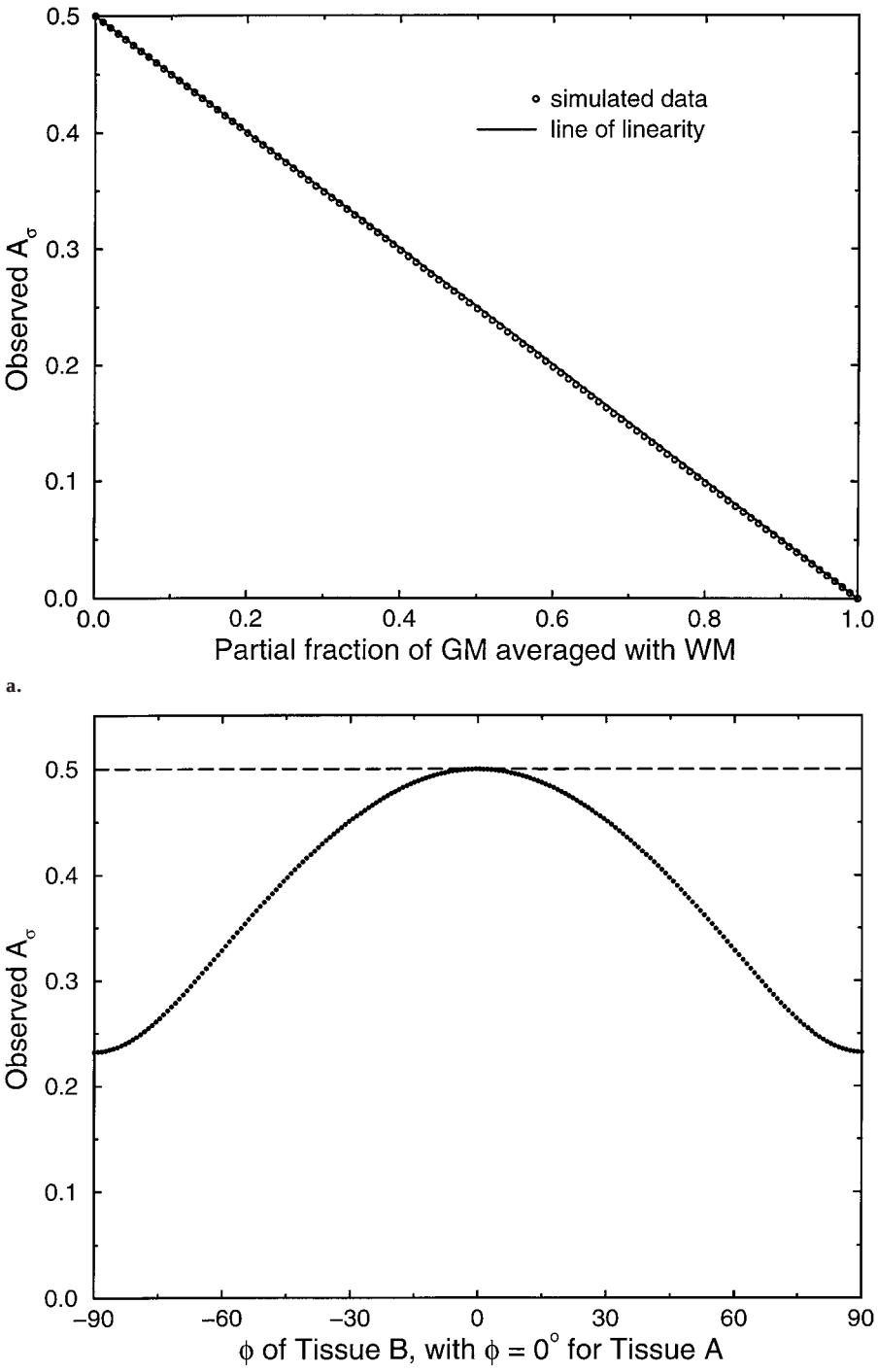

Figure 7. Graphs shows the results of simulation of partial volume effects on measurement of A_σ for **(a)** intravoxel averaging of GM and WM and **(b)** averaging of two WM tissues with unaligned fiber orientations. **(a)** Ideal GM and WM were modeled after the putamen and splenium of the corpus callosum ($\overline{D} = 0.72 \times 10^{-3}$ mm^2/sec for GM and WM, $A_\sigma = 0$ for GM, $A_\sigma = 0.5$ and $A_{minor} = 0$ for WM, and arbitrary settings of $\phi = 20°$ and $\theta = 30°$ for WM). Note the nearly exact linear partial volume effect of GM on WM measurements. **(b)** Two WM tissues, each with the same WM averaged diffusivity ($\overline{D}$) and A_σ values as in **a** and with fibers lying in the transverse imaging plane ($\theta = 0°$), were averaged at different in-plane angular separations (ϕ). Note that angular separations of 90° result in a decrease of more than 50% in the observed A_σ. Dashed line = ideal measurement with no partial volume effect.

and across species is indicative that the data in Tables 1 and 2 can serve as a baseline for comparison with data from diseased brain.

Sorting of the ROIs according to A_σ value (Table 1) reveals a hierarchy of tissue types. The largest A_σ value was seen in the corpus callosum, which belongs to the commissural class of WM. The next largest group of values was seen in the internal capsule and the optic radiations, which belong to the projection class of WM. The association fibers seen in subcortical WM and the external capsule have a still lower set of anisotropy values. This grouping of A_σ values also is suggested in Table 3, where block-diagonal groups of tissue with statistically similar A_σ values generally segregated into these functional tissue classes.

It is interesting that the clinically observed spread of vasogenic edema into these tissue classes has a known similar order of preference, with distribution into association fibers in mild cases and into commissural fibers only in severe cases (46,47). This observation suggests that A_σ may be correlated with resistance to vasogenic fluid spread, possibly owing to dependence on common histologic structural features of WM. The A_σ value and other anisotropy measures may thus be indexes of microscopic architectural characteristics, such as fiber packing density, myelination, order, and/or directional coherence. The sensitivity of A_σ to WM class suggests that, in general, A_σ may be sensitive to changes and abnormalities in WM structure and organization. This sensitivity is supported by results from recent studies of human brain maturation (24,25) and multiple sclerosis (21–23) and other myelination abnormalities (20). The time (approximately 1½ minutes) needed to obtain these data with full brain coverage makes this method practical for clinical applications.

The GM tissues listed in Table 1 (basal ganglia and cortical GM), which are composed mainly of cell bodies, demonstrate an A_σ value consistent with 0 at the SNR levels used in this study. This conclusion is based on the simulation results shown in Figure 6a. Among the ROIs in Table 1 that are consistent with nonzero anisotropy, the thalamus has the smallest A_σ value (see also the simulation results in Fig 6b). Structured anisotropy patterns were present in the thalamus (Figs 2, 5) and likely affected the ROI measurements (Fig 3); thus, the thalamic values should be considered only an average of tissue substructures (eg, nuclei and WM tracts).

The simulation results shown in Figure 6a demonstrate that the bias and noise in GM A_σ values will both be reduced by increasing the SNR of the acquired images (graphed as the SNR of the reference T2-weighted image). Specifically, the A_σ bias and noise are inversely proportional

to the reference SNR (Fig 6a); that is, the SNR and signal-to-bias ratios of A_σ are proportional to the reference SNR. The inverse proportionality between bias and reference SNR is a direct result of the definition of A_σ, where A_σ is, in effect, a measure of the SD of diffusivity measurements in different directions (see Appendix, Eq [A1]). Because the SD of a scalar diffusivity measurement generally is inversely proportional to the reference SNR at typical clinical SNR levels (26,48), there is an overall inverse proportionality between A_σ and the reference SNR.

The simulation results shown in Figure 6b indicate that A_σ bias can also occur in WM measurements and can be reduced by increasing the reference SNR. At a reference SNR of approximately 40–60 (as used in this study), bias becomes significant (ie, greater than the SD of the random noise) for anisotropy measurements of less than 0.05. For the lower input SNRs of 20 and 10, A_σ measurements of less than 0.1 and 0.2, respectively, were predicted to contain significant bias. The curves in Figure 6 can serve as calibrations to adjust WM A_σ measurements on the basis of the input SNR.

The simulation results shown in Figure 6 suggest that acquisition of data with an increased SNR (eg, by means of signal averaging, as in Fig 5) will likely improve the statistical characterization of tissue types, owing to a reduction in A_σ noise and bias. Reduction in bias is particularly relevant to characterization of tissues across institutions and equipment, where SNR levels may differ.

However, the improvements in tissue characterization that can be gained by increases in the SNR may be limited by two factors: (*a*) practical limitations in the number of signals acquired, and (*b*) biologic variability across subjects. The first factor is demonstrated in Figure 6a, which indicates that reductions in A_σ noise and bias that could be achieved by means of averaging would be modest when the input SNR already is high (eg, >50). For example, with a reference T2-weighted MR image SNR of 50:1 without averaging, approximately four signals would need to be acquired and averaged to reduce the bias by a factor of two, from 0.05 to 0.025, and approximately 16 signals would need to be acquired and averaged to reduce the bias by a factor of four to 0.0126. The A_σ noise would be reduced by similar relative amounts. As a corollary, extensive signal acquisition would be necessary to enable detection of low-level GM anisotropy below the detectable level in this study. Such extensive signal acquisition may not be practical in the clinical setting.

The second practical limitation in tissue characterization is variability across subjects. Further analysis of the raw ROI data that contributed to the results given in Table 1 (not shown) indicated that the variation in ROI A_σ values of GM across subjects was dominated by thermal MR noise, with an overall observed SD that was only 1.1–1.7 times that predicted on the basis of thermal MR noise alone. In contrast, for the WM tissues listed in Table 1, the overall SD, across subjects, was 1.5–4.0 times that predicted on the basis of thermal noise alone.

Such variations in measurement that are beyond the thermal noise limit may be due to two factors: biologic variability across subjects and variability in ROI sampling of spatially heterogeneous or small structures. GM measurement variability was near the thermal noise limit, likely because of the spatial homogeneity (Fig 3) and zero anisotropy of the regions, which led to accurate sampling and low biologic variation, respectively. In contrast, the higher variability in WM measurements likely was due to the spatial inhomogeneity and small size of the measured WM structures (Fig 3), which would contribute to sampling errors, and the nonzero anisotropy values, which may be sensitive to biologic differences between subjects. Because the variation in WM A_σ values across subjects was due to factors in addition to thermal noise, increases in the reference SNR alone may have a limited effect on statistical tissue characterization across subjects. If a major component of the WM variability is due to region sampling rather than to biologic differences, measurement variability across subjects may be reduced by trading off a higher SNR for higher spatial resolution.

The images of A_{major} (Fig 2, *b*) have an appearance and noise level similar to those of A_σ (Fig 2, *a*). The rank order of A_{major} across tissue was identical to that of A_σ, both being correlated with WM class (Table 1). In contrast, A_{minor} (Fig 2, *c*) had a different appearance than A_σ and did not correlate well with WM class (Table 1). Regions of higher A_{minor} (eg, genu of the internal capsule) deviated from axisymmetry, possibly because of inhomogeneous fiber orientation and/or spacing. It is possible that the appearance of A_{minor} may be dependent on spatial resolution due to partial volume effects (see Fig 7b). The principal diffusion coefficients $\lambda_{x'}$, $\lambda_{y'}$, and $\lambda_{z'}$ given in Table 2 generally had a ranking that could be correlated with WM tissue class, but the ranking was less characteristic for the thalamus and GM. Also shown in Table 2 is the wide range of values (nearly sixfold) in the principal diffusion coefficients in tissue with high A_σ such as the splenium of the corpus callosum.

Evaluation of partial anisotropy-weighted MR measures (see Appendix, Eqq [A4,A5]) demonstrates their qualitative utility and limitations in cases where the full diffusion tensor is not available. A larger component of the anisotropy resides in the tetrahedral gradient encoding as compared with orthogonal gradient encoding. This is shown qualitatively in Figure 2, *d* and *e*, and quantitatively by comparing the two anisotropy-weighted components in Table 1. The average value of the ratio of AW_{tet} to AW_{ortho} is 2.56, as computed with the data in Table 1. An example of the orientation-dependent deficits predicted earlier (see ''Theory'' in Materials and Methods) for the anisotropy-weighted components is the focal AW_{tet} deficit in the splenium of the corpus callosum (Fig 2, *d*), which was consistent across subjects. The direction of the fibers in this tract is aligned with the y axis ($\theta = 90°$, $\phi = 90°$), a direction in which anisotropy is not expected to be effectively recovered by AW_{tet} on the basis of Figure 4 and Equation (A7) in the Appendix. This focal deficit can, in principle, be partially corrected in the case of a tetrahedral-only acquisition by dividing AW_{tet} by f_{tet} in Equation (A7) in the Appendix, where f_{tet} is computed by using θ and ϕ derived from the tetrahedral data (26). This procedure would be equivalent to generation of the entire diffusion tensor from the tetrahedral data, given the axisymmetric assumption, and then by computing A_σ from Equation (3).

Noticeable deficits also were present on AW_{ortho} MR images, such as the marked reduction in intensity in the lateral genu of the corpus callosum (Fig 2, *e*), where the fibers are oriented toward the tetrahedral directions. However, AW_{ortho} cannot be corrected by dividing by f_{ortho}, in the case of orthogonal-only acquisition, because the data are not sufficient to determine θ and ϕ.

In summary, high-SNR MR diffusion-tensor data were analyzed, and quantitative anisotropy was measured in 13 neurologically healthy adults. Anisotropy, or A_σ, images demonstrated WM anatomy not typically seen on conventional MR images, with statistically significant A_σ differences in different histologic WM classes that were ranked according to known resistance to edema spread, which is suggestive of a sensitivity to WM microstructure. Images of A_σ demonstrated the external capsule; the thickness of the

internal capsule; and substructures of the thalamus, basal ganglia, and occipital white matter, which are not readily seen on conventional MR images. The rotationally invariant A_σ can be calculated directly from the diffusion tensor elements or, as an alternative, directly from the seven diffusion coefficients measured with tetrahedral and orthogonal diffusion encoding. Unlike other anisotropy measures, determination of A_σ does not require diagonalization of the diffusion tensor or sorting of eigenvalues and is on an absolute anisotropy scale of 0–1. Statistically significant differences were found between A_σ values in different histologic classes of WM: From highest to lowest A_σ value, these were commissural WM, projection WM, association WM, and the thalamus. This anisotropy rank was correlated with the known resistance of WM to the spread of vasogenic edema as seen radiologically. Anisotropy measured in the basal ganglia and the cortical GM was consistent with an A_σ value of 0. The ability to distinguish among different histologic classes of cerebral tissue by using anisotropy measurement is suggestive of a sensitivity to microscopic WM fiber structure and may presage the ability to use A_σ to identify WM disease.

APPENDIX

Theory and Computation of Diffusion-Tensor Anisotropy

The A_σ value is a measure of diffusion variation derived from the second moment (variance) of the diffusion tensor D:

$$A_\sigma = \frac{1}{\sqrt{2}}\frac{\sigma(\mathrm{D})}{\overline{D}} = \frac{1}{\sqrt{6}}\frac{\sqrt{Tr[(\mathrm{D}-\overline{D}\mathrm{I})^2]}}{\overline{D}}, \quad \text{(A1)}$$

where I is the unit matrix; *Tr* is the trace of the matrix specified in the brackets, which is given by the sum of its diagonal elements; and σ(D) represents the SD of diffusion coefficients that would be obtained with multiple measurements in different directions. Equation (A1) can be expanded to

$$A_\sigma = \frac{1}{\sqrt{6}\overline{D}}\sqrt{\sum_{i,j=x,y,z}(D_{ij}-\overline{D}\delta_{ij})^2} = \sqrt{A^2_{\mathrm{major}} + \frac{1}{3}A^2_{\mathrm{minor}}}, \quad \text{(A2)}$$

with δ_{ij} representing the Kronecker delta value. The first part of Equation (A2) yields Equation (3). The last part of Equation (A2) is derived by decomposing the diffusion tensor into axisymmetric and nonaxisymmetric parts (26) and expresses A_σ in terms of the major and minor anisotropy values, A_{major} and A_{minor}.

The A_σ value in Equation (A2) can be written as a function of the seven diffusion coefficients measured in the combined tetrahedral-orthogonal approach:

$$A_\sigma = \frac{1}{\sqrt{6}\overline{D}} \times \sqrt{\sum_{i=x,y,z}(D_{ii}-\overline{D})^2 + \frac{9}{8}\sum_{j=1-4}(D_j-\overline{D})^2}, \quad \text{(A3)}$$

where D_1, D_2, D_3, and D_4 are the diffusion coefficients in the tetrahedral directions (26). To assess the anisotropy information contained in the data, A_σ can then be decomposed into partial, noninvariant anisotropy-weighted component measures. Anisotropy weighting can be obtained from the SD of the diagonal elements measured from orthogonal encoding, as proposed by van Gelderen et al (16):

$$AW_{\mathrm{ortho}} = \frac{1}{\sqrt{6}\overline{D}}\sqrt{\sum_{i=x,y,z}(D_{ii}-\overline{D})^2}. \quad \text{(A4)}$$

In similar fashion, anisotropy weighting can be obtained from the SD of the off-diagonal elements contained in Equation (3) and expressed in terms of the tetrahedral diffusion measurements in Equation (A3):

$$AW_{\mathrm{tet}} = \frac{\sqrt{3}}{4\overline{D}}\sqrt{\sum_{j=1-4}(D_j-\overline{D})^2}. \quad \text{(A5)}$$

The full, invariant anisotropy A_σ is obtained by adding the two-component anisotropy-weighted measures in quadrature:

$$A_\sigma = \sqrt{AW^2_{\mathrm{tet}} + AW^2_{\mathrm{ortho}}}. \quad \text{(A6)}$$

In general, A_σ can be computed from Equation (3) by using values of the diffusion-tensor elements that have been globally fit to the entire data set. As an alternative, A_σ can be computed from Equation (A3) by using the diffusion coefficients directly measured at separate orthogonal and tetrahedral experiments. In comparison with the latter approach, the former global analysis procedure constrains the analysis in this overdetermined case (ie, seven diffusion-weighted images that encode seven diffusion coefficients D_1, D_2, D_3, D_4, D_{xx}, D_{yy}, and D_{zz} used to estimate six unknown diffusion-tensor elements). Separate calculation of the diagonal and off-diagonal elements from the orthogonal and tetrahedral data, respectively, would not take advantage of the additional constraint that both methods should yield the same averaged diffusivity (ie, $\overline{D} = {}^1\!/_3[D_{xx} + D_{yy} + D_{zz}] = {}^1\!/_4[D_1 + D_2 + D_3 + D_4]$).

Information Content of Anisotropy-weighted Indexes

Certain WM regions may exhibit symmetry that can simplify the evaluation of the diffusion tensor and provide insight about the information contained in anisotropy-weighted indexes in Equations (A4,A5). Voxels composed of muscle or WM fibers with uniform packing and direction may demonstrate axial or cylindric symmetry. In this approximation, the diffusion ellipsoid is prolate, with diffusivity parallel to the tract that is larger than the diffusivity perpendicular to the tract. Furthermore, the two perpendicular diffusivities would be equal ($A_{\mathrm{minor}} = 0$ and $A_\sigma = |A_{\mathrm{major}}|$); therefore, the rotation angle around the major axis can be set to 0° with no loss of generality. In the axisymmetric approximation, only four scalars are needed to represent the diffusion tensor: the parallel and perpendicular diffusivity and two rotation angles (26,49). In this case, the tetrahedral gradient-encoding method, which is used to acquire diffusion data in four diffusion directions for each voxel, can be used to completely determine the diffusion tensor.

Under conditions of axisymmetry, a direct expression can be written relating A_σ to the off-diagonal diffusion-tensor elements by using equations (16,27c) in Conturo et al (26). However, computation of A_σ with this expression may, in some cases, be unstable, due to division by small off-diagonal elements (data not shown). In contrast, computations of the in-plane angle ϕ and the through-plane angle θ by using equations (27a,27b) in Conturo et al are stable for imaging in humans (30) because of the favorable properties of the arc-tangent function. Thus, a more stable procedure for computation of A_σ from tetrahedral measurements can be devised as follows in the case of axisymmetric diffusion: The A_σ value can be expressed as a function of its anisotropy-weighted tetrahedral component in Equation (A5) and of the angles θ and ϕ, computed with the arc-tangent function. We derive expressions for the fractional recovery of anisotropy contained in the anisotropy-weighted tetrahedral ($f_{\mathrm{tet}}[\theta,\phi]$) and orthogonal ($f_{\mathrm{ortho}}[\theta,\phi]$) components as a ratio of the full A_σ. These ratios are only functions of θ and ϕ:

$$f^2_{\mathrm{tet}}(\theta,\phi) = \frac{AW^2_{\mathrm{tet}}}{A^2_\sigma} = \frac{3}{4}(\sin^4\theta\sin^2 2\phi + \sin^2 2\theta), \quad \text{(A7)}$$

and

$$f^2_{\mathrm{ortho}}(\theta,\phi) = \frac{AW^2_{\mathrm{ortho}}}{A^2_\sigma} = 1 - f^2_{\mathrm{tet}}(\theta,\phi). \quad \text{(A8)}$$

The ratios f_{tet} and f_{ortho} indicate how much of A_σ is recovered in the anisotropy-weighted measures. The expressions in Equations (A7,A8) are specific to the axisymmetric case. Because AW_{tet} can be calculated directly from the tetrahedral diffusion coefficient measurements by using Equation (A5), and θ and ϕ can be calculated under the axisymmetric assumption (26), A_σ can be obtained with Equation (A7) in the axisymmetric case.

Because the averaged diffusivity can be obtained from the tetrahedral or orthogonal gradient-encoding data alone, either encoding method can have clinical applications in cases such as cerebral ischemia. It is thus desirable to analyze what anisotropy-weighted information can be obtained in those cases. The ratios in Equations (A7,A8) are estimates of how much of the total anisotropy A_σ is contained in the separate anisotropy-weighted measurements; that is, in the on- and off-diagonal elements. If the axes of the diffusion ellipsoid are aligned along the coordinate axes, all four

tetrahedral measurements are equivalent, and the full anisotropy is contained in AW_{ortho}. In similar fashion, if the ellipsoid axes are aligned with the tetrahedral directions, the full anisotropy is contained in AW_{tet}.

For axisymmetric diffusion, only the major axis must be aligned for these conditions to be met. Specifically, it can be shown from Equation (A7), in the axisymmetric case, that f_{tet} is 0 at θ values of 0° and 180° (along the z axis) and at θ values of 90° when ϕ is 0°, 90°, 180°, and 270° (along the x or y axis) (see Fig 4a, 4d). Likewise, it can be shown from Equation (A8) that f_{ortho} is 0 at a θ of 54.74° (half the tetrahedral angle) when ϕ is ±45°, ±135° and at θ of 125.26° (180° − 54.74°) when ϕ is ±45°, ±135° (see Fig 4b, 4c). For intermediate alignments, the anisotropy is distributed between the two anisotropy-weighted components, which add in quadrature to yield the full anisotropy value.

References

1. Stejskal EO, Tanner JE. Spin diffusion measurements: spin echoes in the presence of a time dependent field gradient. J Chem Phys 1965; 42:288–292.
2. Le Bihan D, Breton E. Imagerie de diffusion in vivo par résonance magnètique nucléaire. CR Acad Sci Paris 1985; 301:1109–1112.
3. Le Bihan D, Breton E, Lallemand D, Grenier P, Cabanis E, Laval-Jeantet M. MR imaging of intravoxel incoherent motions: application to diffusion and perfusion in neurologic disorders. Radiology 1986; 161:401–407.
4. Taylor DG, Bushell MC. The spatial mapping of translational diffusion coefficients by the NMR imaging technique. Phys Med Biol 1985; 30:345–349.
5. Mansfield P. Multi-planar imaging using NMR spin-echoes. J Phys [C] 1977; 10:L55–L58.
6. Avram H, Crooks L. Effect of self-diffusion on echoplanar imaging (abstr). In: Book of abstracts: Society of Magnetic Resonance in Medicine 1988. Berkeley, Calif: Society of Magnetic Resonance in Medicine, 1988; 980.
7. Turner R, Le Bihan D, Maier J, Vavrek R, Hedges LK, Pekar J. Echo-planar imaging of intravoxel incoherent motion. Radiology 1990; 177:407–414.
8. Turner R, Le Bihan D. Single-shot diffusion imaging at 2.0 Tesla. J Magn Reson 1990; 86:445–452.
9. McKinstry RC, Weisskoff RM, Cohen MS, et al. Instant MR diffusion/perfusion imaging (abstr). In: Book of abstracts: Society of Magnetic Resonance in Medicine 1990. Berkeley, Calif: Society of Magnetic Resonance in Medicine, 1990; 401.
10. Moseley ME, Cohen Y, Kucharczyk J, et al. Diffusion-weighted MR imaging of anisotropic water diffusion in cat central nervous system. Radiology 1990; 176:439–445.
11. Doran M, Hajnal JV, Van Bruggen N, King MD, Young IR, Bydder GM. Normal and abnormal white matter tracts shown by MR imaging using directional diffusion weighted sequences. J Comput Assist Tomogr 1990; 14:865–873.
12. Crank J. The mathematics of diffusion. Oxford, England: Clarendon, 1975.
13. Basser PJ, Mattiello J, Le Bihan D. Estimation of the effective self-diffusion tensor from the NMR spin echo. J Magn Reson B 1994; 103:247–254.
14. Basser PJ, Mattiello J, Le Bihan D. MR diffusion tensor spectroscopy and imaging. Biophys J 1994; 66:259–267.
15. Sorensen AG, Buonanno FS, Gonzalez RG, et al. Hyperacute stroke: evaluation with combined multisection diffusion-weighted and hemodynamically weighted echo-planar MR imaging. Radiology 1996; 199:391–401.
16. van Gelderen P, de Vleeschouwer MH, DesPres D, Pekar J, van Zijl PC, Moonen CT. Water diffusion and acute stroke. Magn Reson Med 1994; 31:154–163.
17. Pierpaoli C, Jezzard P, Basser PJ, Barnett A, Di Chiro G. Diffusion tensor MR imaging of the human brain. Radiology 1996; 201:637–648.
18. Shimony JS, McKinstry RC, Akbudak E, Snyder AZ, Aronovitz JA, Conturo TE. Cerebral diffusion tensor imaging: normative data, signal to noise measurements, and anatomical findings (abstr). In: Proceedings of the Fifth Meeting of the International Society for Magnetic Resonance in Medicine. Berkeley, Calif: International Society for Magnetic Resonance in Medicine, 1997; 225.
19. Shimony JS, McKinstry RC, Akbudak E, Aronovitz JA, Snyder AZ, Conturo TE. Quantitative diffusion tensor anisotropy imaging: normative human cerebral data (abstr). In: Proceedings of the Sixth Meeting of the International Society for Magnetic Resonance in Medicine. Berkeley, Calif: International Society for Magnetic Resonance in Medicine, 1998; 1241.
20. Ono J, Harada K, Mano T, Sakurai K, Okada S. Differentiation of dys- and demyelination using diffusional anisotropy. Pediatr Neurol 1997; 16:63–66.
21. Werring DJ, Clark CA, Barker GJ, et al. The structural properties of multiple sclerosis lesions demonstrated by diffusion tensor imaging (abstr). In: Proceedings of the Sixth Meeting of the International Society for Magnetic Resonance in Medicine. Berkeley, Calif: International Society for Magnetic Resonance in Medicine, 1998; 119.
22. Zhong J, Graham GD, Guarnaccia JB, Hadeishi Y, Gore JC. Quantitative apparent diffusion coefficient and diffusion anisotropy analysis of multiple sclerosis plaques (abstr). In: Proceedings of the Sixth Meeting of the International Society for Magnetic Resonance in Medicine. Berkeley, Calif: International Society for Magnetic Resonance in Medicine, 1998; 1324.
23. Shimony JS, Akbudak E, McKinstry RC, Lori N, Cull TS, Conturo TE. Quantitative diffusion anisotropy imaging: normal values, anatomical findings, and results in relapsing remitting multiple sclerosis (abstr). Radiology 1998; 209(P):240.
24. Neil JJ, Shiran SI, McKinstry RC, et al. Normal brain in human newborns: apparent diffusion and diffusion anisotropy measured by using diffusion tensor MR imaging. Radiology 1998; 209:57–66.
25. Takeda K, Nomura Y, Sakuma H, Tagami T, Okuda Y, Nakagawa T. MR assessment of normal brain development in neonates and infants: comparative study of T1- and diffusion weighted images. J Comput Assist Tomogr 1997; 21:1–7.
26. Conturo TE, McKinstry RC, Akbudak E, Robinson BH. Encoding of anisotropic diffusion with tetrahedral gradients: a general mathematical diffusion formalism and experimental results. Magn Reson Med 1996; 35:399–412.
27. Basser PJ. Inferring microstructural features and the physiological state of tissues from diffusion-weighted images. NMR Biomed 1995; 8:333–344.
28. Basser PJ, Pierpaoli C. Microstructural and physiological features of tissues elucidated by quantitative-diffusion-tensor MRI. J Magn Reson B 1996; 111:209–219.
29. Pierpaoli C, Basser PJ. Toward a quantitative assessment of diffusion anisotropy. Magn Reson Med 1996; 36:893–906.
30. McKinstry RC, Akbudak E, Snyder AZ, Aronovitz JA, Conturo TE. Echo planar human diffusion tensor imaging with tetrahedral encoding (abstr). In: Proceedings of the Fourth Meeting of the International Society for Magnetic Resonance in Medicine. Berkeley, Calif: International Society for Magnetic Resonance in Medicine, 1996; 192.
31. Conturo TE, McKinstry RC, Aronovitz JA, Neil JJ. Diffusion MRI: precision, accuracy and flow effects. NMR Biomed 1995; 8:307–332.
32. Cantor CR, Shimmel PR. Biophysical chemistry part II: techniques for the study of biological structure and function. San Francisco, Calif: Freeman, 1980; 457–458.
33. Reese TG, Weisskoff RM, Smith RN, Rosen BR, Dinsmore RE, Wedeen VJ. Imaging myocardial fiber architecture in vivo with magnetic resonance. Magn Reson Med 1995; 34: 786–791.
34. Basser PJ, Pierpaoli CA. A simplified method to measure the diffusion tensor from seven MR images. Magn Reson Med 1998; 39:928–934.
35. National Electrical Manufacturers Association. Determination of SNR in diagnostic magnetic resonance images. Washington, DC: National Electrical Manufacturers Association, 1988.
36. Mattiello J, Basser PJ, Le Bihan D. The b matrix in diffusion tensor echo-planar imaging. Magn Reson Med 1997; 37:292–300.
37. Le Bihan D. Diffusion and perfusion magnetic resonance imaging: applications to functional MRI. New York, NY: Raven, 1995.
38. Moonen CT, Pekar J, de Vleeschouwer MH, van Gelderen P, van Zijl PC, DesPres D. Restricted and anisotropic displacement of water in healthy cat brain and in stroke studied by NMR diffusion imaging. Magn Reson Med 1991; 19:327–332.
39. Norris DG, Niendorf T, Hoehn-Berlage M, et al. Incidence of apparent restricted diffusion in three different models of cerebral infarction. Magn Reson Imaging 1994; 12:1175–1182.
40. McKinstry RC, Weiskoff RM, Belliveau JW, et al. Ultrafast MR imaging of water mobility: animal models of altered cerebral perfusion. JMRI 1992; 2:377–384.
41. Haselgrove JC, Moore JR. Correction for distortion of echo-planar images used to calculate the apparent diffusion coefficient. Magn Reson Med 1996; 36:960–964.
42. Snyder AZ. Difference image vs ratio image error function forms in PET-PET realignment. In: Myers R, Cunningham V, Bailey D, Jones T, eds. Quantification of brain function using PET. San Diego, Calif: Academic Press, 1995; 131–137.
43. Ojemann JG, Buckner RL, Akbudak E, et al. Functional MRI studies of word stem completion: reliability across laboratories and comparison to blood flow imaging with PET. Hum Brain Mapp 1998; 6:203–215.
44. Bevington P. Data reduction and error analysis for the physical sciences. New York, NY: McGraw-Hill, 1969.
45. DeArmond SJ, Fusco MM, Dewey MM. Structure of the human brain: a photographic atlas. New York, NY: Oxford University Press, 1989.
46. Cowley AR. Dyke award: influence of fiber tracts on the CT appearance of cerebral edema—anatomic-pathologic correlation. AJNR 1983; 4:915–925.
47. Moody DM, Bell MA, Challa VR. The corpus callosum, a unique white-matter tract: anatomic features that may explain sparing in Binswanger disease and resistance to flow of fluid masses. AJNR 1988; 9:1051–1059.
48. Chien D, Buxton RB, Kwong KK, Brady TJ, Rosen BR. MR diffusion imaging of the human brain. J Comput Assist Tomogr 1990; 14:514–520.
49. Hsu EW, Mori S. Analytical expressions for the NMR apparent diffusion coefficients in an anisotropic system and a simplified method for determining fiber orientation. Magn Reson Med 1995; 34:194–200.